AN EXPERIMENTAL AND THEORETICAL STUDY ON THE UTILIZATION OF OBSERVATION CHANNEL FOR TRANSMITTER NOISE CANCELLATION IN IN-BAND FULL-DUPLEX RADIOS

A THESIS SUBMITTED TO
THE GRADUATE SCHOOL OF NATURAL AND APPLIED SCIENCES
OF
MIDDLE EAST TECHNICAL UNIVERSITY

BY

ALTUĞ KAYA

IN PARTIAL FULFILLMENT OF THE REQUIREMENTS
FOR
THE DEGREE OF MASTER OF SCIENCE
IN
ELECTRICAL AND ELECTRONICS ENGINEERING

AUGUST 2022

Approval of the thesis:

AN EXPERIMENTAL AND THEORETICAL STUDY ON THE UTILIZATION OF OBSERVATION CHANNEL FOR TRANSMITTER NOISE CANCELLATION IN IN-BAND FULL-DUPLEX RADIOS

submitted by **ALTUĞ KAYA** in partial fulfillment of the requirements for the degree of **Master of Science in Electrical and Electronics Engineering Department, Middle East Technical University** by,

Prof. Dr. Halil Kalıpçılar
Dean, Graduate School of **Natural and Applied Sciences** _____

Prof. Dr. İlkay Ulusoy
Head of Department, **Electrical and Electronics Engineering** _____

Assist. Prof. Dr. Gökhan Muzaffer Güvensen
Supervisor, **Electrical and Electronics Engineering, METU** _____

Examining Committee Members:

Prof. Dr. Ali Özgür Yılmaz
Electrical and Electronics Engineering, METU _____

Assist. Prof. Dr. Gökhan Muzaffer Güvensen
Electrical and Electronics Engineering, METU _____

Prof. Dr. Umut Orguner
Electrical and Electronics Engineering, METU _____

Prof. Dr. Cenk Toker
Electrical and Electronics Engineering, Hacettepe University _____

Assist. Prof. Dr. Serkan Sarıtaş
Electrical and Electronics Engineering, METU _____

Date: 31.08.2022

I hereby declare that all information in this document has been obtained and presented in accordance with academic rules and ethical conduct. I also declare that, as required by these rules and conduct, I have fully cited and referenced all material and results that are not original to this work.

Name, Surname: Altuğ Kaya

Signature :

ABSTRACT

AN EXPERIMENTAL AND THEORETICAL STUDY ON THE UTILIZATION OF OBSERVATION CHANNEL FOR TRANSMITTER NOISE CANCELLATION IN IN-BAND FULL-DUPLEX RADIOS

Kaya, Altuğ
M.S., Department of Electrical and Electronics Engineering
Supervisor: Assist. Prof. Dr. Gökhan Muzaffer Güvensen

August 2022, 70 pages

Conventional Half-Duplex (HD) systems orthogonalize transmitted and received signals either in time, frequency or both in order not to interfere a signal-of-interest with a transmitted signal. If this interference (also known as self-interference, SI) can be suppressed, a radio can perform simultaneous transmission and reception in the same time & frequency resource and, hence, known as In-Band Full-Duplex (IBFD). IBFD systems potentially double the spectral efficiency compared to their HD counterparts as long as the SI does not saturate the ADC and is suppressed up to the receiver noise floor. However, unlike in HD systems, in IBFD the SI comprises transmitter noise. There are numerous research in literature that offer either propagation domain or analog domain transmitter noise cancellation solutions. Nevertheless, while the former suggestion requires multiple antennas, the latter needs either a bespoke & complex analog circuit design or a transmitter/receiver beamforming or both. In this thesis, an observation receiver is utilized in order to capture the same transmitter noise realization which leakes to the receiver for performing transmitter noise cancellation in the digital domain. To the best of the author's knowledge, this is the first digital domain transmitter noise cancellation technique performed in a nonlinear,

single-antenna hardware setup.

Keywords: In-Band Full-Duplex, Linear Analog Self-Interference Cancellation, Nonlinear Digital Self-Interference Cancellation, Nonlinear Modelling, Generalized Memory Polynomials, Observation Channel, Transmitter Noise Cancellation, Linear Predictor

ÖZ

BANT-İÇİ TAM ÇİFT YÖNLÜ RADYOLARDA GÖZLEM HATTININ VERİCİ GÜRÜLTÜ GİDERİMİ İÇİN KULLANILMASINA YÖNELİK DENEYSEL VE TEORİK BİR ÇALIŞMA

Kaya, Altuğ
Yüksek Lisans, Elektrik ve Elektronik Mühendisliği Bölümü
Tez Yöneticisi: Dr. Öğr. Üyesi. Gökhan Muzaffer Güvensen

Ağustos 2022 , 70 sayfa

Geleneksel Yarı Çift Yönlü sistemler, iletilen sinyalle ilgilenilen sinyali engellememek için iletilen ve alınan sinyalleri zaman, frekans veya her ikisinde de dikgenleştirir. Bu girişim (öz girişim olarak da bilinir) bastırılabilirse, bir radyo aynı zaman & frekans kaynağında eşzamanlı iletim ve alım gerçekleştirebilir ve bu radyolar Bant-İçi Tam Çift Yönlü olarak bilinirler. Bant-İçi Tam Çift Yönlü sistemler, öz girişimi alıcı gürültü tabanına kadar bastırdığı ve öz girişim ADC'yi doyurmadığı sürece Yarı Çift Yönlü benzerlerine kıyasla potansiyel olarak spektral verimliliği iki katına çıkarırlar. Ancak Yarı Çift Yönlü sistemlerden farklı olarak Bant-İçi Tam Çift yönlü sistemler, öz girişimleri içerisinde verici gürültüsünü de barındırır. Literatürde yayılım veya analog bölgede verici gürültü giderimi çözümü sunan birçok araştırma vardır. Bununla birlikte, yayılım bölgesindeki öneriler birden fazla anten gerektirirken analog bölgesindekiler ise ya özel & karmaşık analog devre tasarımına ya gönderici/alıcı hüzme oluşturmaya ya da her ikisine de ihtiyaç duyar. Bu tezde, verici hattından alma hattına sızan aynı gerçeklenişe sahip verici gürültüsünü bir gözlem hattı ile yakala-

yıp sayısal bölgede verici gürültüsü giderimi sağlayacağız. Yazarın bilgisi dahilinde bu yöntem doğrusal olmayan tek antenli donanım kurulumlarında gerçekleştirilen ilk sayısal bölge verici gürültüsü giderme tekniğidir.

Anahtar Kelimeler: Bant-İçi Tam Çift Yönlü, Doğrusal Analog Öz Girişim Giderimi, Doğrusal Olmayan Sayısal Öz Girişim Giderimi, Doğrusal Olmayan Modelleme, Genelleştirilmiş Hafıza Polinomları, Gözlem Hattı, Verici Gürültüsü Giderimi, Doğrusal Kestirici

To my beloved family

ACKNOWLEDGMENTS

Firstly, I would like to thank Assist. Prof. Gökhan Muzaffer Güvensen for his supervision & endless support during my studies. Whenever I directed my questions to him or asked for his guidance, he provided his valuable time. Thus, I give my deepest gratitude to him. Moreover, he motivated me during times when I needed the most. Without him, I was not able to come this far.

Secondly, I would like to thank my mom & dad and my fiancé Yeliz for their unconditional support in life and for being extra considerate during my last year of master's. Their invaluable support has the greatest role in all the success I had. I am deeply thankful to have them.

My special thanks to ASELSAN Inc. for supporting my master's. They encouraged me to attend all of my courses despite the workload in the office. Furthermore, they provided the necessary hardware to pursue my research goals. I appreciate my former team leader Soner Yeşil for introducing In-Band Full-Duplex technology and making enlightening conversations. Sincere thanks to my former colleague Hasan Aykut Şatana. He spared his time for hardware debugging on numerous occasions when I required his expertise. In addition, he allowed me to use one of his MATLAB libraries for sending signals to and receiving from ADRV9375, a key component in the hardware setup. I also would like to thank my colleagues Cansu Şen, Burak Gürtunca, Alper Bereketli, and Elif Karakaya for keeping company during coffee breaks and post-lunch walks. I thank my manager Tolga Numanoğlu for letting me work in highly flexible working hours especially for the last three months. Last but not least, I would like to thank Anıl Kurt and Murat Babek Salman for discussing conceptual and code-level questions.

TABLE OF CONTENTS

LIST OF TABLES

TABLES

LIST OF FIGURES

FIGURES

LIST OF ABBREVIATIONS

ADC	Analog to Digital Converter
API	Application Programmming Interface
ASIC	Analog Self-Interference Cancellation
BER	Bit Error Rate
CP	Cyclic Prefix
CS	Cyclic Suffix
DAC	Digital to Analog Converter
DPD	Digital Predistortion
DSIC	Digital Self-Interference Cancellation
DSP	Digital Signal Processing
FD	Full-Duplex
FDD	Frequency Division Duplex
fLMS	Filtered Least Mean Squares
FPGA	Field-Programmable Gate Array
GMP	Generalized Memory Polynomials
HD	Half-Duplex
IBFD	In-Band Full-Duplex
IFFT	Inverse Fast Fourier Transform
ISI	Inter-Symbol Interference
LMS	Least Mean Squares
LO	Local Oscillator
LS	Least Squares
LTI	Linear Time-Invariant

METU	Middle East Technical University
MP	Memory Polynomial
OFDM	Orthogonal Frequency-Division Multiplexing
PA	Power Amplifier
PSD	Power Spectral Density
RF	Radio Frequency
RSI	Residual Self-Interference
RVTDNN	Real-Valued Time Delay Neural Network
SI	Self-Interference
SIC	Self-Interference Cancellation
SINR	Signal-to-Interference-plus-Noise Ratio
SNR	Signal-to-Noise Ratio
SoI	Signal-of-Interest
TDD	Time Division Duplex

NOMENCLATURE

Scalars

μ	Upsampling ratio of the OFDM symbols for generating narrowband OFDM symbols
μ^{ss}	Step size of the adaptive ASIC algorithm
f_s	Sampling rate of the DAC in the hardware setup
N^{CP}	Number of samples for cyclic prefix
N^{CS}	Number of samples for cyclic suffix
N^{sym}	Number of nonzero subcarriers in an OFDM symbol which are selected from a M-QAM constellation
N^{Win}	Number of samples for rising/falling edge window

Vectors

$\boldsymbol{\beta}^{RxObs}$	GMP coefficients for nonlinearly modelling the observation receiver
$\boldsymbol{\beta}^{Rx}$	GMP coefficients for nonlinearly modelling the ASIC output
$\eta_b^{Rx}[n]$	n^{th} sample of the receiver noise which affects the b^{th} received symbol
$\eta_b^{Tx}[n]$	n^{th} sample of the transmitter noise which affects the b^{th} transmitted symbol
$\hat{H}^{AUX}[k]$	k^{th} subcarrier of the estimated auxiliary transmitter channel in frequency domain
$\hat{h}^{AUX}[n]$	n^{th} tap of the estimated auxiliary transmitter channel impulse response
$\mathbf{X}^{Full}[k]$	An array holding the k^{th} subcarrier of the $0^{th}, \cdots, B-1^{th}$ transmitted fullband OFDM symbols in frequency domain

$\mathbf{Y}^{Full}[k]$	An array holding the k^{th} subcarrier of the $0^{th}, \cdots, B-1^{th}$ received fullband OFDM symbols in frequency domain
$\phi(x_b^+[n])$	n^{th} sample of the RSI component of $\mathbf{y}_b^{Rx,+}[n]$
$\widehat{\widetilde{x}}_b^+[n]$	n^{th} sample of the b^{th} transmitted OFDM symbol consists of CP&CS&Window in time domain which is the output of the nonlinear PA estimate in the synthetic environment
$\widehat{v}_b^{Rx,+}[n]$	n^{th} estimated sample of the nonlinear modelling error of b^{th} received OFDM symbol consists of CP&CS&Window in time domain
$\widetilde{\eta}_b^{Tx}[n]$	n^{th} sample of the raised transmitter noise which affects the b^{th} transmitted symbol
$\widetilde{x}_b^+[n]$	n^{th} sample of the b^{th} transmitted OFDM symbol consists of CP&CS&Window in time domain which is the output of the nonlinear PA
$h^{AUX}[n]$	n^{th} tap of the auxiliary transmitter channel impulse response
$h^{SI}[n]$	n^{th} tap of the SI channel impulse response
$h^{SoI}[n]$	n^{th} tap of the SoI channel
$r_b^+[n]$	n^{th} sample of the b^{th} received OFDM symbol consists of CP& CS&Window in time domain which comes from a distant wireless communication system
$s_b^{Rx,+}[n]$	n^{th} sample of the nonlinearly modelled b^{th} received OFDM symbol consists of CP&CS&Window in time domain
$s_b^{RxObs,+}[n]$	n^{th} sample of the nonlinearly modelled b^{th} received OFDM symbol from the observation receiver consists of CP&CS&Window in time domain
$s_b^{SoI,+}[n]$	n^{th} sample of the b^{th} transmitted OFDM symbol consists of CP&CS&Window in time domain which is sent from a distant wireless communication system
$v_b^{Rx,IQcorr,+}[n]$	n^{th} IQ correlated sample of the nonlinear modelling error of b^{th} received OFDM symbol consists of CP&CS&Window in time domain

$v_b^{Rx,IQdecorr,+}[n]$	n^{th} IQ uncorrelated sample of the nonlinear modelling error of b^{th} received OFDM symbol consists of CP&CS&Window in time domain
$v_b^{Rx,IQdecorr}[n]$	n^{th} IQ uncorrelated sample of the CP&CS&Window-free nonlinear modelling error of b^{th} received OFDM symbol in time domain
$v_b^{Rx,+}[n]$	n^{th} sample of the nonlinear modelling error of b^{th} received OFDM symbol consists of CP&CS&Window in time domain
$v_b^{RxObs,IQcorr,+}[n]$	n^{th} IQ correlated sample of the nonlinear modelling error of b^{th} received OFDM symbol from the observation receiver consists of CP&CS&Window in time domain
$v_b^{RxObs,IQdecorr,+}[n]$	n^{th} IQ uncorrelated sample of the nonlinear modelling error of b^{th} received OFDM symbol from the observation receiver consists of CP&CS&Window in time domain
$v_b^{RxObs,IQdecorr}[n]$	n^{th} IQ uncorrelated sample of the CP&CS&Window-free nonlinear modelling error of b^{th} received OFDM symbol from the observation receiver in time domain
$v_b^{RxObs,+}[n]$	n^{th} sample of the nonlinear modelling error of b^{th} received OFDM symbol from the observation receiver consists of CP& CS&Window in time domain
$v_b^{RxObs}[n]$	n^{th} sample of the CP&CS&Window-free nonlinear modelling error of b^{th} received OFDM symbol from the observation receiver in time domain
$v_b^{Rx}[n]$	n^{th} sample of the CP&CS&Window-free nonlinear modelling error of b^{th} received OFDM symbol in time domain
$w^{ASIC}[n]$	n^{th} tap of the ASIC filter
$w_I^{RxObs}[n]$	n^{th} tap of the IQ Decorrelator filter in observation receiver for inphase terms
$w_I^{Rx}[n]$	n^{th} tap of the IQ Decorrelator filter in receiver for inphase terms
$w_Q^{RxObs}[n]$	n^{th} tap of the IQ Decorrelator filter in observation receiver for quadrature terms

$w_Q^{Rx}[n]$	n^{th} tap of the IQ Decorrelator filter in receiver for quadrature terms
$w_{(i)}^{ASIC}[n]$	n^{th} tap of the adaptive ASIC filter for the i^{th} batch of OFDM symbols
$x_b[n]$	n^{th} sample of the CP&CS&Window-free b^{th} transmitted OFDM symbol in time domain
$x_b^+[n]$	n^{th} sample of the b^{th} transmitted OFDM symbol consists of CP&CS&Window in time domain
$x_b^{Filt,+}[n]$	n^{th} sample of the b^{th} transmitted OFDM symbol consists of CP&CS&Window in time domain which is filtered by $\mathbf{h}^{AUX}$
$x_b^{Filt}[n]$	n^{th} sample of the CP&CS&Window-free b^{th} transmitted OFDM symbol in time domain which is filtered by $\mathbf{h}^{AUX}$
$y_b^{AUX,+}[n]$	n^{th} sample of the b^{th} received OFDM symbol consists of CP& CS&Window in time domain which cancels the SI signal
$y_b^{Rx,+}[n]$	n^{th} sample of the b^{th} received OFDM symbol consists of CP& CS&Window after ASIC in time domain
$y_b^{RxObs,+}[n]$	n^{th} sample of the b^{th} received OFDM symbol from the observation receiver consists of CP&CS&Window in time domain
$y_b^{RxObs}[n]$	n^{th} sample of the CP&CS&Window-free b^{th} received OFDM symbol from the observation receiver in time domain
$y_b^{Rx}[n]$	n^{th} sample of the CP&CS&Window-free b^{th} received OFDM symbol after ASIC in time domain
$y_b^{SI,+}[n]$	n^{th} sample of the b^{th} OFDM symbol consists of CP&CS& Window in time domain which causes SI
$y_b^{SI}[n]$	n^{th} sample of the CP&CS&Window-free b^{th} OFDM symbol in time domain which causes SI
$y_{b,(i)}^{SI}[n]$	n^{th} sample of the CP&CS&Window-free b^{th} OFDM symbol from the i^{th} batch of OFDM symbols in time domain which causes SI

Matrices

$\mathbf{\Phi}(\mathbf{x}_b)$	Matrix containing the GMP basis functions for $\mathbf{x}_b$ in its columns
$\mathbf{\Phi}(\mathbf{x}_b^+)$	Matrix containing the GMP basis functions for $\mathbf{x}_b^+$ in its columns
$\mathbf{V}_b^{RxObs,+}$	Toeplitz matrix containing $\mathbf{v}_b^{RxObs,+}$ in its columns
$\mathbf{V}_b^{RxObs}$	Toeplitz matrix containing $\mathbf{v}_b^{RxObs}$ in its columns
$\mathbf{X}_b$	Toeplitz matrix containing $\mathbf{x}_b^{Filt}$ in its columns
$\mathbf{X}_b^+$	Toeplitz matrix containing $\mathbf{x}_b^{Filt,+}$ in its columns
$\mathbf{X}_{b,(i)}$	Toeplitz matrix containing $\mathbf{x}_b^{Filt}$ from the i^{th} batch of OFDM symbols in its columns

CHAPTER 1

INTRODUCTION

1.1 Motivation

"It is generally not possible for radios to receive and transmit on the same frequency band because of the interference that results" [1]

This quote of Andrea Goldsmith inherits the assumption of radios can either transmit or receive in a given time and frequency resource. This operation mode is known as half-duplex (HD) and HD systems can orthogonalize transmitted and received signals either in time, frequency or both, as in Figure 1.1(a), (b) and (c), respectively [2]. However, a radio can utilize the same time & frequency resource for both transmitted and received signals by suppressing and/or cancelling the more powerful transmitted signal (self-interference, SI) from the much weaker received signal (signal-of-interest, SoI), as in Figure 1.1(d). Such an operation mode that utilizes the same time & frequency resource is known as In-Band Full-Duplex (IBFD). Even though some papers in the field will refer to this concept as "full-duplex" (FD), in this chapter and onwards the IBFD abbreviation is adopted to prevent misunderstanding.

Ideal IBFD systems promise to double the spectral efficiency of single-hop links compared to conventional HD systems. However, the advantages of IBFD systems are not limited to the physical layer and, in fact, the true benefit of it lies in the upper layers of the OSI Reference Model [3], [4–7]. In the literature, both non real-time and real-time MAC layer techniques that take advantage of IBFD can prevent many hidden terminal scenarios and enhance fairness [8–10]. Nevertheless, in this thesis we are focusing on the physical layer aspects of IBFD systems.

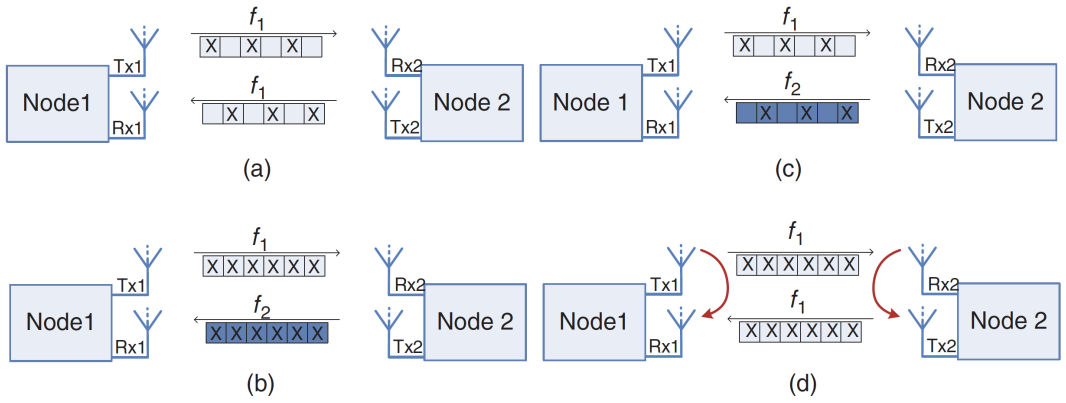

Figure 1.1: Duplex schemes: (a) Time Division Duplex (TDD); (b) Frequency Division Duplex (FDD); (c) Half-Duplex FDD; (d) In-Band Full-Duplex [2].

Different self-interference cancellation (SIC) techniques both in propagation, analog, and digital domain were proposed by the researchers at Middle East Technical University (METU) [11], Stanford [12], Rice [13, 14], and various other groups [10, 15–17]. The motivation of this thesis is to employ the single-antenna hardware setup and the suggested SIC algorithms in [11] at higher average antenna transmit powers than before, to show the problems of transmitter noise creates on IBFD systems, and then to utilize the observation receiver for transmitter noise cancellation.

1.2 Problem Definition

In conventional HD systems having diversity either in time, frequency or both (as in Figure1.1(a), (b) and (c)) eases the hardware design by abstracting the transmitter noise. Although the transmitter noise is present in any system and dependent on the output power level and the receiver gain stage, due to the diversity in time and/or frequency in HD systems, a hardware designer does not have to take any precautions on the transmitter noise itself. However, in IBFD systems, while the more powerful transmitted signal is suppressed/cancelled from the much weaker received signal in propagation, analog and digital domain, the aforementioned transmitter noise should also suppressed/cancelled.

Figure 1.2 and Table 1.1 describe the required amount of SIC in an arbitrary IBFD

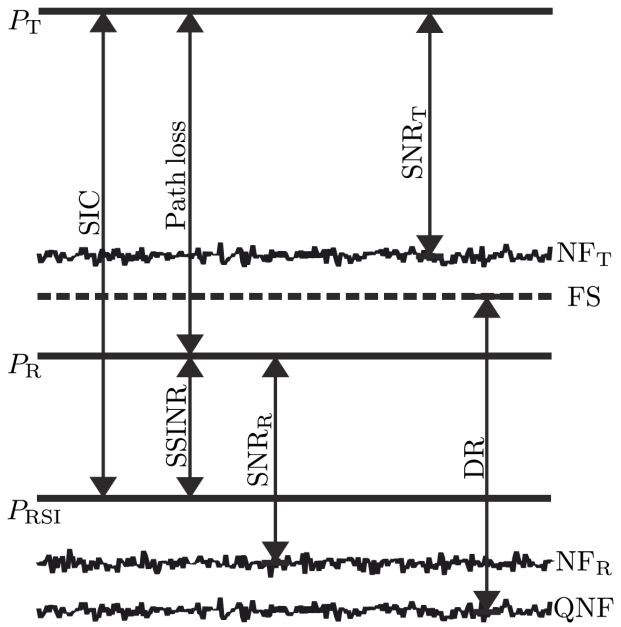

Figure 1.2: A pictorial description of dependencies between the full-duplex transceiver specification on the power chart [15].

Table 1.1: Descriptions of the abbreviations in Figure 1.2.

P_T	Power level of the transmitted signal (SI)
NF_T	Transmitter noise floor
SNR_T	Signal-to-noise ratio in the transmitter
P_R	Power level of the desired reception (SoI)
NF_R	Receiver noise floor
SNR_R	Signal-to-noise ratio in the receiver
FS	Full scale of the ADC
DR	Dynamic range of the ADC
QNF	Quantization noise floor (practically $\sim$6 dB below the NF_R [18])
P_{RSI}	Power level of the residual SI after the SIC
$SSINR$	Signal-to-self-interference-plus-noise-ratio

transceiver pictorially. In Figure1.2 SIC represents SICs in propagation, analog, and digital domains. It is important to note that after the SIC in propagation and analog domains the residual SI power, P_{RSI}, should not saturate the receiver. Furthermore, in order to achieve theoretical $\sim 2\times$ throughput after the SIC in all domains P_{RSI} should be as close as possible to the receiver noise floor, NF_R. In other words, if $SSINR < SNR_R$ in a IBFD system then the throughput efficiency is going to be lower than the theoretical upper bound. Nevertheless, such a system can still be exploited due to higher layer advantages of IBFD systems [4–7].

In Figure 1.2 illustrates and [12] states the transmitter noise floor stands higher than the receiver noise floor and thus, in general, the SI can only be partially cancelled [19]. In two-antenna IBFD systems, the power of the transmitter noise at the receiver is dependent mostly on the amount of antenna separation, for example a two-antenna system can supply more than 40 dB passive cancellation only by separating the antennas from each other [13, 20]. However, in a single-antenna IBFD system, circulators can only supply 20 dB or less passive cancellation [12,21]. In single-antenna IBFD literature [12] and [15], it is argued that the random nature of the transmitter noise disallows the development of an algorithm to cancel it; the former suggests an analog cancellation by splitting the ordinary transmission chain into two and the latter proposes a passive cancellation stage. However, the proposed passive cancellation stage in [15] also suppresses the transmission signal thus affects the link budget negatively and the analog cancellation in [12] requires a sophisticated analog circuit design and calibration stage. In another research a transmission noise aware analog-digital hybrid SIC algorithm is proposed [22]. However, the proposed method is a fully theoretical one and considers linear SIC both in analog and digital domains. In IBFD literature, especially the ones that employs hardware to verify their SIC algorithms, the necessity of nonlinear SIC is well established [10, 12, 15, 23–26].

1.3 Proposed Methods and Contributions

When the nonlinear, single-antenna hardware setup and the suggested SIC algorithms in [11] are analyzed at higher average antenna transmit powers than previously studied, transmitter noise starts to leak to the receiver side and limits the suggested SIC

algorithms. In order to operate the nonlinear, single-antenna hardware setup near the theoretical $\sim 2\times$ throughput region of IBFD systems, the observation receiver on the current hardware setup is utilized for capturing the power amplifier (PA) output on the ordinary transmission chain. The decision of utilizing an observation receiver channel for transmitter noise cancellation was made after rebuilding a simplified hardware setup and analyzing it in the simulation environment.

The proposed method of transmitter noise cancellation is built on top of the suggested algorithms in [11]. First, the PA in the ordinary chain is modelled through observation channel by using nonlinear modelling via Generalized Memory Polynomials (GMP) [27] and the transmitter noise is estimated by the fact that it is nothing but a modelling error. Then, the noise estimate is decontaminated from IQ Imbalance by using a IQ Decorrelator filter operating in real-field as the used hardware setup is a direct conversion system. It is essential to have a residual SI (RSI) that is eliminated from IQ Imbalance effect, because it is a significant and one of the most problematic hardware impairment [28,29] and a serious problem for nonlinear Digital Self-Interference Cancellation (DSIC) [30] including transmitter noise cancellation. Finally, the transmitter noise estimation is then used to predict the RSI (after linear Analog Self-Interference Cancellation (ASIC) and nonlinear DSIC) for performing transmitter noise cancellation by exploiting the fact that the observation and ordinary receiver channels contain the same transmitter noise realization. To the best of the author's knowledge, this is the first digital domain transmitter noise cancellation technique performed in a nonlinear, single-antenna hardware setup.

1.4 The Outline of the Thesis

A transmit signal model is given in Chapter 2, where linear ASIC, nonlinear DSIC, and IQ Decorrelator algorithms are overviewed and evaluated in the hardware setup under the same model with a lower average transmit antenna power. Then, the hardware setup is driven with higher average transmit antenna power and transmitter noise is discovered in Chapter 3. After that, in Chapter 4, the hardware setup is simulated in a synthetic environment with transmitter noise and a transmitter noise cancellation algorithm is proposed and its performance is evaluated from Power Spectral Density

(PSD) plots. Last but not least in Chapter 5, the performance of the proposed transmitter noise cancellation algorithm is evaluated in different average transmit antenna powers via bit error rate (BER) of different SoI signal-to-noise ratios (SNR). Finally, the advantages and disadvantages of the proposed algorithm is discussed in Chapter 6.

Throughout the thesis, the signals containing cyclic prefix (CP), cyclic suffix (CS), and window are shown with a "plus" notation in the superscript ($\square_b^{\square,+}[n]$). In all SIC algorithms, in training phases, filter coefficients are found by using CP&CS &Window-free signals. Then, in testing phases, the SIC signal processing blocks are applied to the signals containing CP&CS&Window. Furthermore, power levels in all PSD plots are denoted by relative units in order to pictorially indicate the amount of SIC in the in-band. Last but not least, in all hardware diagrams discrete-time baseband equivalent model is used before and after ADCs&DACs and up&down converters in the hardware are not shown.

CHAPTER 2

OVERVIEW OF THE SELF-INTERFERENCE CANCELLATION ALGORITHMS AND EVALUATION IN HARDWARE SETUP

In this chapter, previously suggested linear ASIC and nonlinear DSIC algorithms in [11] are overviewed under Orthogonal Frequency-Division Multiplexing (OFDM) signal model. Then, as the used hardware setup is a direct conversion system, an IQ Decorrelator signal processing block is proposed for a hardware impairment called IQ Imbalance. Lastly, the performance of the algorithms is evaluated from Power Spectral Density (PSD) plots by using a nonlinear, single-antenna hardware setup, where the average antenna transmit power is ≈ 10 dBm. The details of the hardware setup is presented in Section 2.5.

2.1 Transmit Signal Model

In this thesis, a block transmission of OFDM modulation is considered, please refer to Figure 2.1. First the information bits are mapped to a unit average power M-QAM constellation and $X_b[k]$, where $k = 0, \cdots, N^{sym} - 1$ number of subcarriers are generated for the b^{th} OFDM symbol. In total there are B number of OFDM blocks

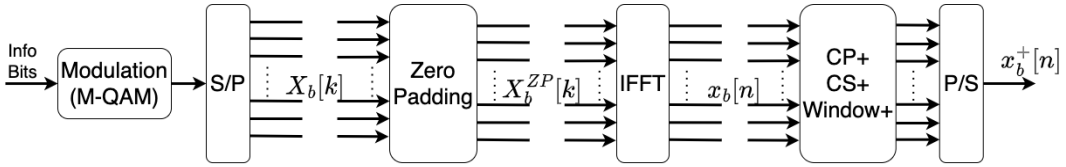

Figure 2.1: A pictorial description of transmit signal generation under OFDM Signal Model.

("Block" and "Symbol" are two words that are used interchangeably throughout the thesis). Then, the subcarriers are parallelized and $N^{sym}(\mu - 1)$ number of zeros are padded as it is shown in (2.1) to generate $\frac{f_s}{\mu}$ bandwidth signal, where f_s is the sampling rate of the Digital to Analog Converter (DAC) in Hz, μ is the upsampling ratio, and μN^{sym} is a power of two:

$$X_b^{ZP}[k] = \begin{cases} X_b[k], \text{ for } 0 \leq k < \frac{N^{sym}+1}{2} \\ 0, \text{ for } \frac{N^{sym}+1}{2} \leq k < \mu N^{sym} - \frac{N^{sym}-1}{2} \\ X_b[k - N^{sym}(\mu - 1)], \text{ for } \mu N^{sym} - \frac{N^{sym}-1}{2} \leq k < \mu N^{sym} \end{cases} \tag{2.1}$$

After the Inverse Fast Fourier Transform (IFFT), a μN^{sym} samples long time domain OFDM signal (hereinafter only "OFDM symbol"), $x_b[n]$, is generated as it is shown in (2.2):

$$x_b[n] = \frac{1}{N^{sym}} \sum_{k=0}^{\mu N^{sym}-1} X_b^{ZP}[k] e^{j2\pi kn} \text{ for } 0 \leq n < \mu N^{sym}. \tag{2.2}$$

When two-sided Inter-Symbol Interference (ISI) is present, estimating a linear channel/filter in frequency domain requires not only a Cyclic Prefix (CP) but also a Cyclic Suffix (CS) [31], details of which are present in Section 2.2.1. Thus, N^{CP} samples are copied from the rear portion of the OFDM symbol, $x_b[n]$, and inserted to the beginning of the same symbol and N^{CS} samples are copied from the front portion of the OFDM symbol, $x_b[n]$, and inserted to the end of the same symbol. The CP&CS inserted OFDM symbol, $x_b^{CPCS}[n]$, is shown in (2.3):

$$x_b^{CPCS}[n] = \begin{cases} x_b[n + \mu N^{sym}], \text{ for } -N^{CP} \leq n < 0 \\ x_b[n], \text{ for } 0 \leq n < \mu N^{sym} \\ x_b[n - \mu N^{sym}], \text{ for } \mu N^{sym} \leq n < \mu N^{sym} + N^{CS} \end{cases} \tag{2.3}$$

In addition, to create smooth transitions between consecutive OFDM symbols, each OFDM symbol should be windowed. Those smooth transitions are required for not causing spectral regrowth [32]. In this thesis study, Hanning window is used which is

shown in (2.4):

$$w[n] = \frac{1}{2}\Big[1 - cos\Big(\frac{2n\pi}{2N^{Win}-1}\Big)\Big], \text{for } 0 \leq n < 2N^{Win}. \tag{2.4}$$

Both the rising and falling edges of the window are N^{Win} samples long. The OFDM symbol that consists of CP&CS&Window, $x_b^+[n]$, is generated mathematically as it is shown in (2.5). The pictorial description of addition of CP&CS&Window is shown in Figure 2.2.

$$x_b^+[n] = \begin{cases} x_b^{CPCS}[n]w[n+N^{CP}], \text{for } -N^{CP} \leq n < N^{Win} - N^{CP} \\ x_b^{CPCS}[n], \text{for } N^{Win} - N^{CP} \leq n < \mu N^{sym} + N^{CS} - N^{Win} \\ x_b^{CPCS}[n]w[n-\mu N^{sym} - N^{CS} + 2N^{Win}], \text{for } \mu N^{sym} + N^{CS} - N^{Win} \leq \\ \qquad\qquad\qquad\qquad\qquad\qquad\qquad\qquad\qquad\qquad n < \mu N^{sym} + N^{CS} \end{cases} \tag{2.5}$$

It is important to note that $N^{Win} < \min(N^{CP}, N^{CS})$ and $\min(N^{CP}, N^{CS}) - N^{Win} \geq L^{Ch}$ where $2L^{Ch}+1$ is the length of the SI channel $h^{SI}[n]$ for $n = -L^{Ch}, \cdots, L^{Ch}$. More details about the SI channel is in Section 2.2.

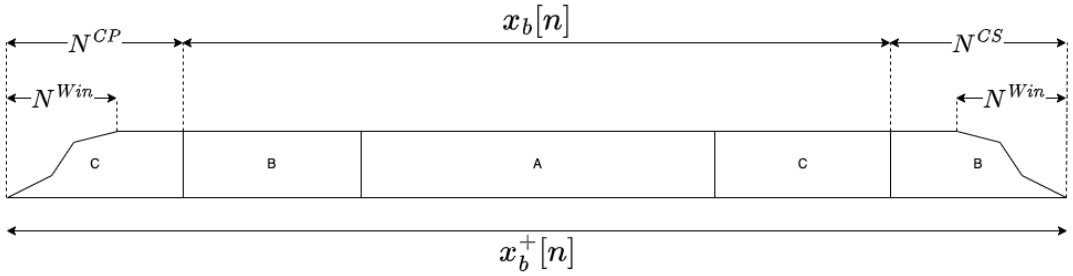

Figure 2.2: Visualisation of an OFDM symbol consists of CP&CS&Window.

2.2 Digitally Controlled Linear Analog Self-Interference Cancellation Algorithm under OFDM Signal Model

In IBFD radios, the power difference between SI and SoI could be around 100 dB [33]. Excessive power of SI can easily go beyond ADC's dynamic range and can saturate receiver [2]. To avoid the saturation of the receiver chain, SIC either in propagation domain, analog domain or both is required. In fact, having SIC only in propagation domain and avoiding the saturation of the ADC is not enough to get a P_{RSI} level that is practical for an IBFD system. In most, if not every, IBFD systems requires some type of Analog SIC (ASIC) for achieving a lower P_{RSI} level [34].

For example, a contemporary femto-cell cellular system can transmit at 21 dBm with a receiver noise floor of -100 dBm as shown in Figure 2.3. If it is assumed that the transmitter and receiver chains are isolated around 15 dB in propagation domain, the SI will be around at 6 dBm and >100 dB SIC is still required for doubling the spectral efficiency and having a nearly ideal IBFD system. Let's assume that the IBFD femto-cell employs a B-bit ADC with $ENOB$ number of effective bits. Then, the effective dynamic range of the ADC becomes $6.02(ENOB - 2)$ dB as 1-bit is spared for clipping and 1-bit is reserved for avoiding a quantization limited system. For example,

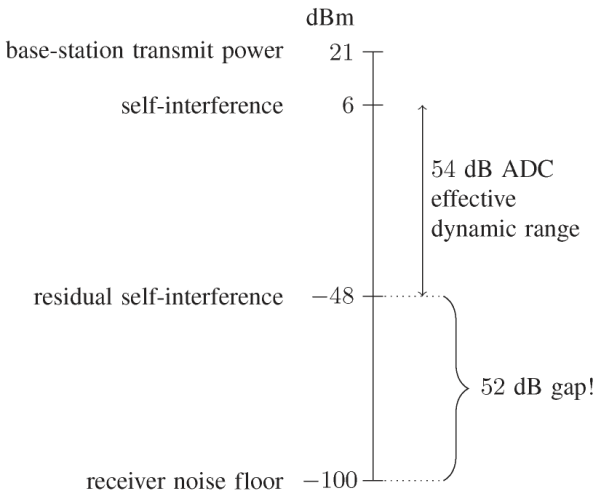

Figure 2.3: Illustrative example of residual SI motivated by contemporary femto-cell cellular systems [34].

if the IBFD femto-cell utilizes an AD9683 [35] from Analog Devices ($ENOB = 11$-bits) then the effective dynamic range becomes 54 dB. Any type of DSIC can only suppress the SI up to the effective dynamic range, and thus in this example, even with a perfect DSIC P_{RSI} level would be 52 dB above the desired receiver noise floor [34]. To conclude, ASIC before the ADC is strongly recommended in IBFD systems.

In this thesis a nonlinear, single-antenna hardware setup is used where propagation domain SIC is realized by a circulator and analog domain SIC is obtained by an auxiliary transmission chain:

- A circulator is a three-port passive RF component that routes the transmitted signal from the transmitter chain to the antenna and from antenna to the receiver chain, as it is shown in Figure 2.4 [36]. An ideal circulator does not allow the transmitted signal to leak to the receiver port, directly. However, practically, it cannot suppress the de-routed signal completely. Instead, it applies 20 dB or less passive suppression (also known as isolation) between the transmitter and receiver ports [12, 21].

- In auxiliary chain SIC method, the transmitted signal is generated via an additional transmitter chain from scratch starting from its baseband IQ samples. Then, the transmitted signal is fed to the receiver directly, without propagating through air-interface, in order to be subtracted from the total received signal [2], as it is shown in Figure 2.5.

In the hardware setup, details of which are presented in Section 2.5, there are two transmitter chains and two receiver chains, as it is shown in Figure 2.6. The first transmitter chain (Tx) is the ordinary chain for transmitting signals to other nodes. It consists of a high gain nonlinear Power Amplifier (PA). The second transmitter

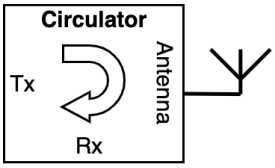

Figure 2.4: Schematic of a circulator in circuit diagrams.

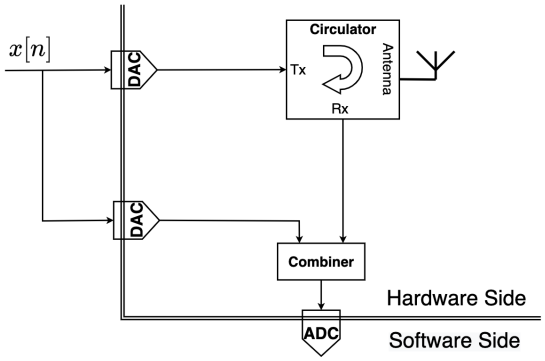

Figure 2.5: Pictorial description of a simplified Auxiliary Chain SIC Method.

chain (TxAux) is the auxiliary transmission chain for generating the ASIC signal. It consists of a low gain linear PA. The first receiver chain (Rx) is the ordinary receiver chain for receiving SoI from other nodes. However, in addition to the SoI, the SI will also leak to the ordinary receiver chain. The second receiver chain (RxObs) is called the observation channel and it is used to observe the nonlinear PA at the ordinary transmitter chain. Then the Digital Predistortion (DPD) engine in the AD9375 runs a pruned implementation of generalized memory polynomials (GMP) to model a large number of PA characteristics such as weak nonlinearities, temperature variation, and memory effects [37]. DPD is used to linearize the output of the PA and increase the

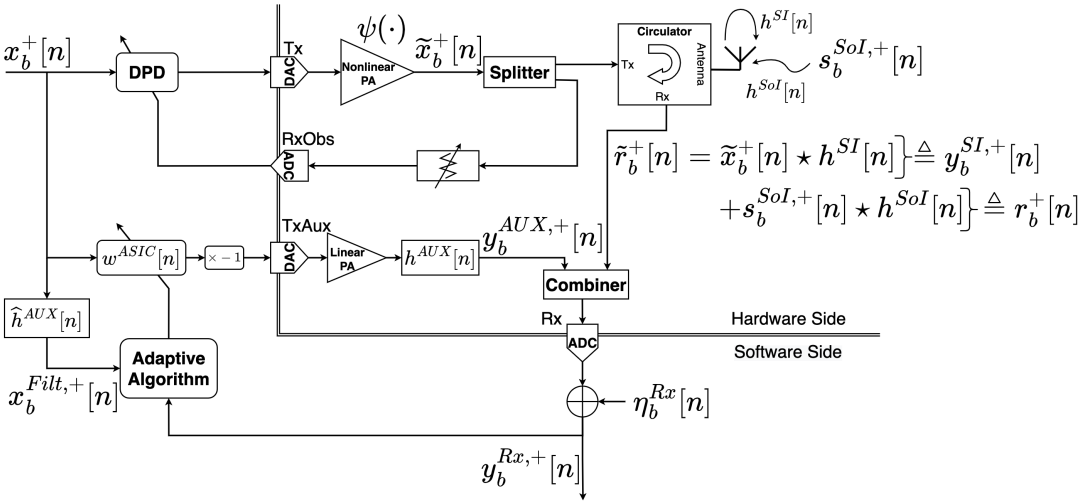

Figure 2.6: A diagram that shows linear ASIC signal processing block and hardware components. The "plus" notation in the superscript of the signals ($\square_b^{\square,+}[n]$) represents the existence of CP&CS&Window.

efficiency of the PA. Linearization corresponds to not occupying adjacent channels, please refer to Section 2.6 for DPD activated and deactivated Power Spectral Density (PSD) plots of OFDM signals.

In Figure 2.6, the auxiliary transmitter channel, $h^{AUX}[n]$, makes the conventional Least Mean Squares (LMS) algorithm fail to find the adaptive ASIC filter, $w^{ASIC}[n]$, because the error signal is represented by both $w^{ASIC}[n]$ and $h^{AUX}[n]$. In such a situation, the coefficients of the adaptive ASIC filter cannot be found alone. Thus in [11], a method known as Filtered Least Mean Squares (fLMS) is invoked to track the channel variations in the SI channel, $h^{SI}[n]$. In this method, the filtered input signal, $x_b^{Filt,+}[n]$, is used in the adaptive algorithm. fLMS is widely used in echo cancellation implementations [38] and it enables the convergence of $w^{ASIC}[n]$, where the adaptive filter is initiated by an unit impulse in discrete time. To derive the coefficient update formulation of $w^{ASIC}[n]$, one should estimate the $h^{AUX}[n]$ first and then invoke the commutative property of Linear Time-Invariant (LTI) systems.

2.2.1 Auxiliary Channel Estimation

The auxiliary channel is assumed to be constant throughout the OFDM symbol blocks and it is estimated in frequency domain by a maximum likelihood estimator using fullband OFDM symbols. The FFT is used to transform the time domain signal into frequency domain. CP&CS insertion at the transmitter and removal at the receiver guarantees circularly symmetric convolution matrix generation for noncausal channels [31]. Thus, the b^{th} fullband OFDM symbol passed through the auxiliary channel can be written in the frequency domain as shown in (2.6):

$$Y_b^{Full}[k] = X_b^{Full}[k]H^{AUX}[k] + N_b^{Rx}[k], \tag{2.6}$$

where k stands for the subcarriers, $N_b^{Rx}[k] \sim CN(0, \sigma_{Rx}^2)$ is the additive white complex-valued thermal noise in the frequency domain. The joint probability mass function of $\left(\mathbf{Y}^{Full}[k], H^{AUX}[k] \middle| \mathbf{X}^{Full}[k]\right)$ is shown in (2.7), where $\mathbf{Y}^{Full}[k] = \left[Y_0^{Full}[k], \cdots, Y_{B-1}^{Full}[k]\right]$ and $\mathbf{X}^{Full}[k] = \left[X_0^{Full}[k], \cdots, X_{B-1}^{Full}[k]\right]$:

$$\mathrm{p}\Big(\mathbf{Y}^{Full}[k], H^{AUX}[k]\Big|\mathbf{X}^{Full}[k]\Big) = \prod_{b=0}^{B-1} \frac{1}{\sqrt{2\pi\sigma_{Rx}^2}} \exp\Bigg(\frac{-1}{2\sigma_{Rx}^2}\Big|Y_b^{Full}[k] - X_b^{Full}[k]H^{AUX}[k]\Big|^2\Bigg). \quad (2.7)$$

Maximizing the likelihood is equal to minimizing the negative log-likelihood as it is shown in (2.8):

$$\frac{\partial \ln\Big(\mathrm{p}\Big(\mathbf{Y}^{Full}[k], H^{AUX}[k]\Big|\mathbf{X}^{Full}[k]\Big)\Big)}{\partial H^{AUX}[k]^*} = \sum_{b=0}^{B-1} \Big(Y_b^{Full}[k] - X_b^{Full}[k]H^{AUX}[k]\Big)X_b^{Full}[k]^* \triangleq 0. \quad (2.8)$$

Then, the frequency domain auxiliary channel that minimizes the log-likelihood functions can be estimated as in (2.9), assuming that the auxiliary channel is static across OFDM symbols even between batches (Please refer to Figure 2.7). The time domain auxiliary channel estimate, $\hat{h}^{AUX}[n]$, can be found by means of IFFT.

$$\hat{H}^{AUX}[k] = \frac{\sum_{b=0}^{B-1} Y_b^{Full}[k]X_b^{Full}[k]^*}{\sum_{b=0}^{B-1} X_b^{Full}[k]X_b^{Full}[k]^*} \text{ for } \forall k. \quad (2.9)$$

2.2.2 ASIC Filter Coefficient Update through Minimizing the Block-Averaged Mean Squared Error

The ASIC filter, $w^{ASIC}[n]$, should track the channel variations in SI channel $h^{SI}[n]$, where $n = -L^{Ch}, \cdots, L^{Ch}$. Thus, $w^{ASIC}[n]$ should also be a noncausal filter, where $n = -L^{Filt}, \cdots, L^{Filt}$ and $L^{Filt} \leq L^{Ch}$. When the auxiliary channel is estimated and the commutative property of the LTI systems is invoked, the filtered transmission signal can be written as in (2.10). The $\star$ represents convolution operation:

$$x_b^{Filt,+}[n] = x_b^{+}[n] \star \widehat{h}^{AUX}[n]. \quad (2.10)$$

When there is no SoI in Figure 2.6, the ASIC output $y_b^{Rx,+}[n]$ (error containing CP&CS&Window) can be written as in (2.11):

$$\mathbf{e}_b^+ \triangleq \mathbf{y}_b^{Rx,+} = \mathbf{y}_b^{SI,+} - \mathbf{X}_b^+ \mathbf{w}^{ASIC}, \tag{2.11}$$

where $\mathbf{X}_b^+$ is a Toeplitz (convolution) matrix containing $\mathbf{x}_b^{Filt,+}$ in its columns and $\mathbf{w}^{ASIC} = \Big[w^{ASIC}\big[-L^{Filt}\big], \cdots, w^{ASIC}\big[L^{Filt}\big]\Big]^T$. Minimization of Block-Averaged Mean Squared Error via Least Squares (LS) method will reveal the $w^{ASIC}[n]$, as it is shown in (2.12)-(2.14). In this thesis, CP&CS&Window-free signals are used in every training (also known as finding filter coefficient) phase in order to discard any two-sided ISI. Thus, $\mathbf{X}_b$ is the convolution matrix containing $x_b^{Filt}[n]$ in its columns. In addition, all the training phases use M number of OFDM blocks, where $M \leq B$, to find the coefficients of signal processing blocks.

$$\frac{\partial E_b\Big\{\mathbf{e}_b^H \mathbf{e}_b\Big\}}{\partial \mathbf{w}^{ASIC^H}} = \frac{\partial E_b\Big\{\big(\mathbf{y}_b^{SI^H} - \mathbf{w}^{ASIC^H}\mathbf{X}_b^H\big)\big(\mathbf{y}_b^{SI} - \mathbf{X}_b\mathbf{w}^{ASIC}\big)\Big\}}{\partial \mathbf{w}^{ASIC^H}}, \tag{2.12}$$

$$E_b\Big\{-\mathbf{X}_b^H\big(\mathbf{y}_b^{SI} - \mathbf{X}_b\mathbf{w}^{ASIC}\big)\Big\} = -E_b\Big\{\mathbf{X}_b^H\mathbf{y}_b^{SI}\Big\} + E_b\Big\{\mathbf{X}_b^H\mathbf{X}_b\Big\}\mathbf{w}^{ASIC} \triangleq 0, \tag{2.13}$$

$$\Rightarrow \mathbf{w}^{ASIC} = \left(\sum_{b=0}^{M-1}\mathbf{X}_b^H\mathbf{X}_b\right)^{-1}\left(\sum_{b=0}^{M-1}\mathbf{X}_b^H\mathbf{y}_b^{SI}\right). \tag{2.14}$$

In (2.14) $\mathbf{X}_b$ is a Toeplitz matrix (containing $\mathbf{x}_b^{Filt}$ in its columns) of size $(\mu N^{sym} - 2L^{Filt}) \times (2L^{Filt}+1)$, $\mathbf{y}_b^{SI}$ is of size $(\mu N^{sym} - 2L^{Filt}) \times 1$, and thus $\mathbf{w}^{ASIC}$ is of size $(2L^{Filt}+1) \times 1$. An adaptive LS algorithm can be built on top of (2.14) by introducing a step-size, μ^{ss}, as in shown in (2.15):

$$\mathbf{w}_{(i+1)}^{ASIC} = \mathbf{w}_{(i)}^{ASIC} + \mu^{ss}\left(\sum_{b=0}^{M-1}\mathbf{X}_{b,(i+1)}^H\mathbf{X}_{b,(i+1)}\right)^{-1}\left(\sum_{b=0}^{M-1}\mathbf{X}_{b,(i+1)}^H\mathbf{y}_{b,(i+1)}^{SI}\right), \tag{2.15}$$

where the subscripts i and $i+1$ represents batch numbers in Figure 2.7. The adaptive LS can track the channel variations in SI channel between batches. As it is shown

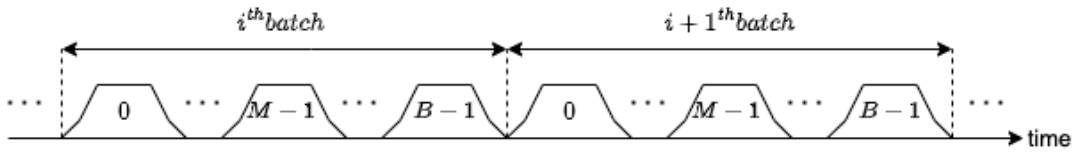

Figure 2.7: Pictorial description of consecutive batches of OFDM Symbols consists of CP&CS&Window.

in Figure 2.7, each batch contains B number of OFDM symbols and M number of them are used in training phase and in the training phase trained filters are applied to all B number of blocks in the same batch, as it is shown in (2.11). However, due to the hardware limitations, finite many OFDM symbols can be captured in a batch at once by the hardware. Thus, the adaptive LS algorithm updates the ASIC Filter Coefficients for the $i+1^{th}$ batch, $w_{(i+1)}^{ASIC}[n]$, by using the ASIC Filter Coefficients for the i^{th} batch, $w_{(i)}^{ASIC}[n]$. Adaptive LS approach is also used in the synthetic environment.

In the implementation of (2.15) pseudo-inverse operation, `pinv()`, is used other than the inverse operation, `inv()`, as $\mathbf{X}_{b,(i+1)}^{H}\mathbf{X}_{b,(i+1)}$ becomes close to singular due to narrowband, and thus correlated, $\mathbf{x}_b^{Filt}$.

2.2.3 Received Signal Model after ASIC

The received signal at the Rx Port (please refer to Figure 2.6) can be written as it is shown in (2.16), when the desired signal, $s_b^{SoI,+}[n]$, is present in the system:

$$y_b^{Rx,+}[n] \triangleq \phi(x_b^+[n]) + r_b^+[n] + \eta_b^{Rx}[n], \tag{2.16}$$

$$\begin{aligned} \phi(x_b^+[n]) &\triangleq y_b^{SI,+}[n] + y_b^{AUX,+}[n], \\ y_b^{SI,+}[n] &= \widetilde{x}_b^+[n] \star h^{SI}[n], \\ y_b^{AUX,+}[n] &= -x_b^+[n] \star w^{ASIC}[n] \star h^{AUX}[n], \end{aligned} \tag{2.17}$$

$$r_b^+[n] \triangleq s_b^{SoI,+}[n] \star h^{SoI}[n], \tag{2.18}$$

where the first term in (2.16) represents the residual SI after the ASIC (details are in (2.17)), the second term represents the received SoI (details are in (2.18)), and the third term represents the additive white complex-valued thermal noise $\sim CN(0, \sigma_{Rx}^2)$.

2.3 Nonlinear Digital Self-Interference Cancellation Algorithm under OFDM Signal Model

The proposed ASIC algorithm described in Section 2.2 and shown in Figure 2.6 is a linear ASIC technique as a linear PA is used and there are no nonlinear component present in the auxiliary transmitter chain. In order to increase the effectiveness of the ASIC, nonlinear PA in the ordinary transmitter chain, $\psi(\cdot)$, is linearized by the built-in DPD in the AD9375. The DPD in the AD9375 is based on a pruned implementation of Generalized Memory Polynomials (GMP) to linearize the output of the nonlinear PA [37]. However, at higher PA output powers and under strong nonlinearity the DPD cannot linearize the PA completely [39]. Thus, the RSI component of the received signal at the Rx Port after the linear ASIC in (2.16) and (2.17), $\phi(x_b^+[n])$, contains both linear and nonlinear components of SI.

The nonlinear DSIC algorithm uses GMP basis functions to model the nonlinear SI, expressions of basis functions can be found in Appendix A [27]. The modelling of nonlinear SI is shown in (2.19):

$$\mathbf{y}_b^{Rx,+} = \mathbf{\Phi}(\mathbf{x}_b^+)\boldsymbol{\beta}^{Rx} + \mathbf{v}_b^{Rx,+}, \tag{2.19}$$

where $\boldsymbol{\beta}^{Rx}$ is a vector containing GMP coefficients and $\mathbf{\Phi}(\mathbf{x}_b^+)$ is a matrix containing the GMP basis functions for $\mathbf{x}_b^+$ in its columns, and $\mathbf{v}_b^{Rx,+}$ represents the modelling error. In Figure 2.8, pictorial description of nonlinear modelling is shown. According to (2.19) $s_b^{Rx,+}[n] \triangleq \mathbf{\Phi}(x_b^+[n])\boldsymbol{\beta}^{Rx}$ and $v_b^{Rx,+}[n] = y_b^{SI,+}[n] - s_b^{Rx,+}[n]$. In the training phase CP&CS&Window-free M number of blocks (from the same batch) are used to minimize the Block-Averaged MSE via LS to find the GMP coefficients, $\boldsymbol{\beta}^{Rx}$. Please refer to (2.20)-(2.22):

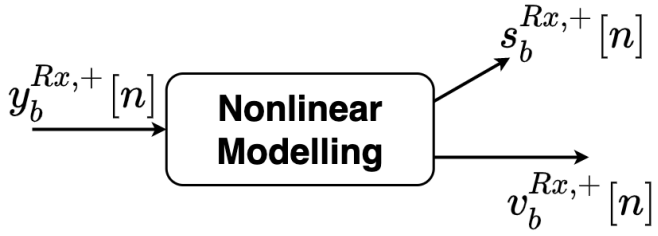

Figure 2.8: Pictorial description of the nonlinear DSIC algorithm. The "plus" notation in the superscript of the signals ($\square_b^{\square,+}[n]$) represents the existence of CP&CS&Window.

$$\frac{\partial E_b\Big\{\Big|\mathbf{v}_b^{Rx}\Big|^2\Big\}}{\partial \boldsymbol{\beta}^{Rx^H}} = \frac{\partial E_b\Big\{\big(\mathbf{y}_b^{Rx^H} - \boldsymbol{\beta}^{Rx^H}\boldsymbol{\Phi}(\mathbf{x}_b)^H\big)\big(\mathbf{y}_b^{Rx} - \boldsymbol{\Phi}(\mathbf{x}_b)\boldsymbol{\beta}^{Rx}\big)\Big\}}{\partial \boldsymbol{\beta}^{Rx^H}}, \tag{2.20}$$

$$E_b\Big\{ - \boldsymbol{\Phi}(\mathbf{x}_b)^H\big(\mathbf{y}_b^{Rx} - \boldsymbol{\Phi}(\mathbf{x}_b)\boldsymbol{\beta}^{Rx}\big)\Big\} = \\ - E_b\Big\{\boldsymbol{\Phi}(\mathbf{x}_b)^H\mathbf{y}_b^{Rx}\Big\} + E_b\Big\{\boldsymbol{\Phi}(\mathbf{x}_b)^H\boldsymbol{\Phi}(\mathbf{x}_b)\Big\}\boldsymbol{\beta}^{Rx} \triangleq 0, \tag{2.21}$$

$$\Rightarrow \boldsymbol{\beta}^{Rx} = \left(\sum_{b=0}^{M-1}\boldsymbol{\Phi}(\mathbf{x}_b)^H\boldsymbol{\Phi}(\mathbf{x}_b)\right)^{-1}\left(\sum_{b=0}^{M-1}\boldsymbol{\Phi}(\mathbf{x}_b)^H\mathbf{y}_b^{Rx}\right). \tag{2.22}$$

In (2.22) the matrix $\boldsymbol{\Phi}(\mathbf{x}_b)$ containing the GMP basis function for triplet (k,l,m) in its columns. The basis function is $x_b\big[n-l\big]\Big|x_b\big[n-l-m\big]\Big|^k$, where $k = 0,\cdots,K^{GMP}$ and $l = -L^{GMP},\cdots,L^{GMP}$ and $m = -M^{GMP},\cdots,M^{GMP}$. $\boldsymbol{\Phi}(\mathbf{x}_b)$ is of size $(\mu N^{sym} - 2L^{GMP} - 2M^{GMP}) \times (K^{GMP}(2L^{GMP}+1)(2M^{GMP}+1) + (2L^{GMP}+1))$, $\mathbf{y}_b^{Rx}$ is of size $(\mu N^{sym} - 2L^{GMP} - 2M^{GMP}) \times 1$ and hence, $\boldsymbol{\beta}^{Rx}$ becomes of size $(K^{GMP}(2L^{GMP}+1)(2M^{GMP}+1) + (2L^{GMP}+1)) \times 1$.

In (2.22) the column size of $\boldsymbol{\Phi}(\mathbf{x}_b)$ is not equal to $(K^{GMP}+1)(2L^{GMP}+1)(2M^{GMP}+1)$, because when $k = 0$, each l should be used to calculate the column of $\boldsymbol{\Phi}(\mathbf{x}_b)$ only once. If each l is used with each m, then $\boldsymbol{\Phi}(\mathbf{x}_b)$ becomes rank deficient and the inverse operation becomes undefined. In addition, in the implementation of (2.22)

pseudo-inverse operation, `pinv()`, is used other than the inverse operation, `inv()`, as $\mathbf{\Phi}(\mathbf{x}_b)^H\mathbf{\Phi}(\mathbf{x}_b)$ becomes close to singular due to narrowband, and thus correlated, $\mathbf{x}_b$.

In testing phase shown in (2.19), $\mathbf{\Phi}(\mathbf{x}_b^+)$ is generated where the matrix is of size $(\mu N^{sym} + N^{CP} + N^{CS}) \times (K^{GMP}(2L^{GMP}+1)(2M^{GMP}+1) + (2L^{GMP}+1))$. Then $\mathbf{\Phi}(\mathbf{x}_b^+)$ is used to generate $\mathbf{s}_b^{Rx,+} = \mathbf{\Phi}(\mathbf{x}_b^+)\boldsymbol{\beta}^{Rx}$ and the error signal becomes $\mathbf{v}_b^{Rx,+} = \mathbf{y}_b^{SI,+} - \mathbf{s}_b^{Rx,+}$.

2.4 IQ Decorrelator Algorithm under OFDM Signal Model

The output of the nonlinear DSIC algorithm, $v_b^{Rx,+}[n]$, is affected by a hardware impairment called IQ Imbalance, as the hardware setup presented in Section 2.5 is a direct conversion system. The IQ Imbalance contaminates the in-band and acts like a residual SI (RSI). The IQ Imbalance effect on the spectrum is arbitrarily shown in Figure 2.9 and further details can be found in Appendix B.

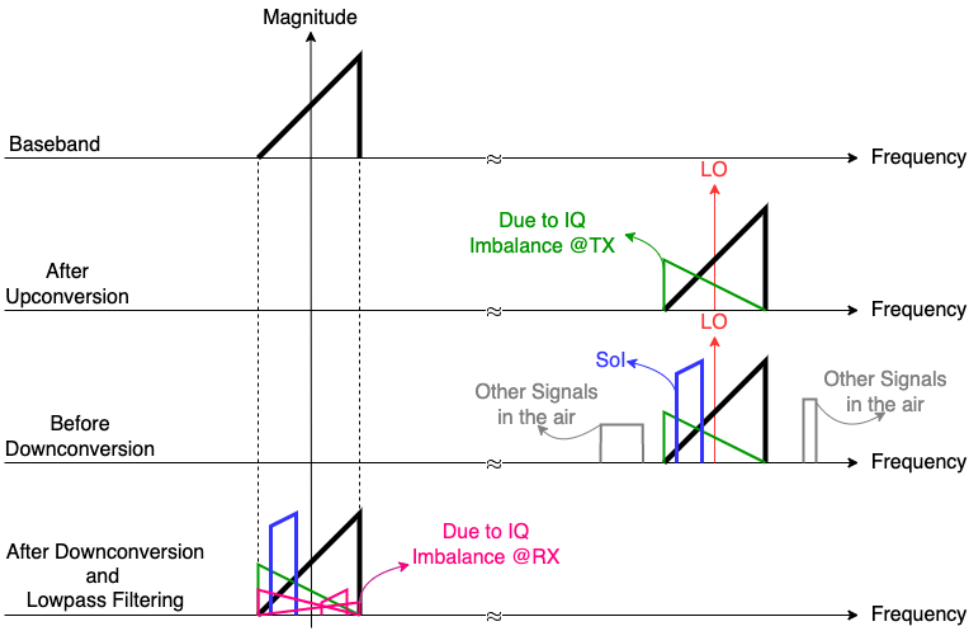

Figure 2.9: Pictorial description of IQ Imbalance impairment on the spectrum by arbitrarily chosen signals. Bandwidth of the SoI is purposefully narrowed to fully describe the IQ Imbalance on transmitter and receiver chains.

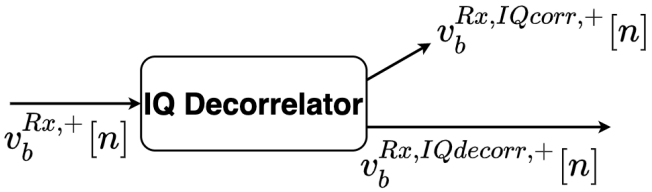

Figure 2.10: Pictorial description of IQ Decorrelator algorithm. The "plus" notation in the superscript of the signals ($\square_b^{\square,+}[n]$) represents the existence of CP&CS&Window.

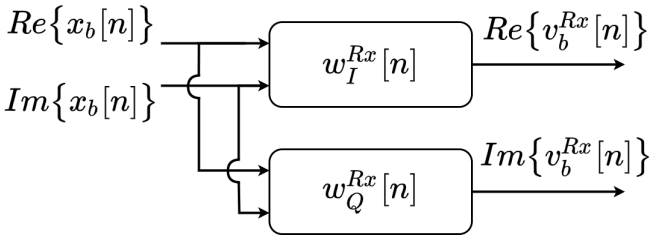

Figure 2.11: Pictorial description of two-input one-output linear predictors.

The shown IQ Decorrelator in Figure 2.10 is based on two-input one-output linear predictors that operate in the real-field. Input vector $\mathbf{a}_b[n] = \Big[Re\{x_b[n]\}, Im\{x_b[n]\}\Big]$ is of size 1×2 and used to estimate $Re\{v_b^{Rx}[n]\}$ and $Im\{v_b^{Rx}[n]\}$ separately, as it is shown in Figure 2.11. In the training phase CP&CS&Window-free M number of blocks (from the same batch) are used to minimize the Block-Averaged MSE via LS to find the IQ Decorrelator filter coefficients, $w_I^{Rx}[n]$ and $w_Q^{Rx}[n]$. Please refer to (2.23)-(2.25) for finding IQ Decorrelator filter coefficients, where $\mathbf{A}_b$ is a Toeplitz matrix (containing $\mathbf{a}_b[n]$ in its columns):

$$\frac{\partial E_b\Big\{\Big|Re\{\mathbf{v}_b^{Rx,IQdecorr}\}\Big|^2\Big\}}{\partial \mathbf{w}_I^{Rx^T}} = \frac{\partial E_b\Big\{Re\{\mathbf{v}_b^{Rx^T} - \mathbf{w}_I^{Rx^T}\mathbf{A}_b^T\}Re\{\mathbf{v}_b^{Rx} - \mathbf{A}_b\mathbf{w}_I^{Rx}\}\Big\}}{\partial \mathbf{w}_I^{Rx^T}}, \tag{2.23}$$

$$E_b\Big\{-\mathbf{A}_b^T\big(Re\{\mathbf{v}_b^{Rx}\} - \mathbf{A}_b\mathbf{w}_I^{Rx}\big)\Big\} = -E_b\Big\{\mathbf{A}_b^T Re\{\mathbf{v}_b^{Rx}\}\Big\} + E_b\Big\{\mathbf{A}_b^T\mathbf{A}_b\Big\}\mathbf{w}_I^{Rx} \triangleq 0, \tag{2.24}$$

$$
\begin{aligned}
\Rightarrow \mathbf{w}_I^{Rx} &= \left(\sum_{b=0}^{M-1} \mathbf{A}_b^T \mathbf{A}_b\right)^{-1} \left(\sum_{b=0}^{M-1} \mathbf{A}_b^T Re\{\mathbf{v}_b^{Rx}\}\right). \\
\Rightarrow \mathbf{w}_Q^{Rx} &= \left(\sum_{b=0}^{M-1} \mathbf{A}_b^T \mathbf{A}_b\right)^{-1} \left(\sum_{b=0}^{M-1} \mathbf{A}_b^T Im\{\mathbf{v}_b^{Rx}\}\right).
\end{aligned} \tag{2.25}
$$

In (2.25) $\mathbf{A}_b$ is of size $(\mu N^{sym} - 2L^{IQ}) \times (2(2L^{IQ}+1))$, $\mathbf{v}_b^{Rx}$ is of size $(\mu N^{sym} - 2L^{IQ}) \times 1$, and thus $\mathbf{w}_I^{Rx}$ and $\mathbf{w}_Q^{Rx}$ are of size $(2(2L^{IQ}+1)) \times 1$.

In the testing phase the Toeplitz matrix $\mathbf{A}_b^+$ of size $(\mu N^{sym} + N^{CP} + N^{CP}) \times (2(2L^{IQ}+1))$ is generated, where it contains $\mathbf{a}_b^+[n] = \Big[Re\{x_b[n]^+\}, Im\{x_b[n]^+\}\Big]$ in its columns. Then the outputs of the IQ Decorrelator signal block shown in Figure 2.10 can be written as in (2.26):

$$
\begin{aligned}
\mathbf{v}_b^{Rx,IQcorr,+} &= \mathbf{A}_b^+ \mathbf{w}_I^{Rx} + j\mathbf{A}_b^+ \mathbf{w}_Q^{Rx}, \\
\mathbf{v}_b^{Rx,IQdecorr,+} &= \mathbf{v}_b^{Rx,+} - \mathbf{v}_b^{Rx,IQcorr,+}.
\end{aligned} \tag{2.26}
$$

After the linear ASIC, nonlinear DSIC, and IQ Decorrelator DSP blocks, CP&CS& Window can be removed from the error signal of IQ Decorrelator, $v_b^{Rx,IQdecorr}[n] \approx RSI + r_b^+[n] + \eta_b^{Rx}[n]$, and then it can be equalized and demodulated to obtain the information bits that the SoI carries.

2.5 Details of the Hardware Setup

In Figure 2.12, input&output relationship of previously explained linear ASIC, nonlinear DSIC, and IQ Decorrelator algorithms are summarized. The hardware components in Figure 2.12 are exactly used in the hardware setup shown in Figure 2.13. The hardware setup, containing off-the-shelf components other than the antenna, is based on an ADRV9375 Evaluation Board [37] which hosts a highly integrated, wideband RF transceiver called AD9375 [39]. It offers dual-channel transmitter and receivers, a fully integrated DPD adaptation engine (based on a pruned implementation of GMP), and digitally controlled analog attenuation/gain stages for transmitter/re-

ceiver chains. However, AD9375 employs two different built-in frequency synthesizers for the transmitter and receiver chains. To limit the oscillator phase noise impairment, a common local oscillator (LO) is used [2]. ADF4372 LO Generator [40] is used to fed the common LOs to external LO ports of the transmitter and receiver chains. Moreover, as the user guide of ADRV9375 suggests, a networking-capable carrier board Xilinx ZC706 is included in the setup. An application programming interface (API) is used in the MATLAB environment to configure the ADRV9375 Evaluation Board (mixer settings, DPD activation/deactivation, how many samples to capture, etc.), to send baseband signals to the upconverters, and to receive baseband signals from the downconverters through an Ethernet cable. It is important to note that the transmitted and received baseband signals are processed in MATLAB via the signal processing blocks shown in Figure 2.12, other than the DPD.

Carrier frequency and sampling rate (f_s) of the ADRV9375 Evaluation Board is set

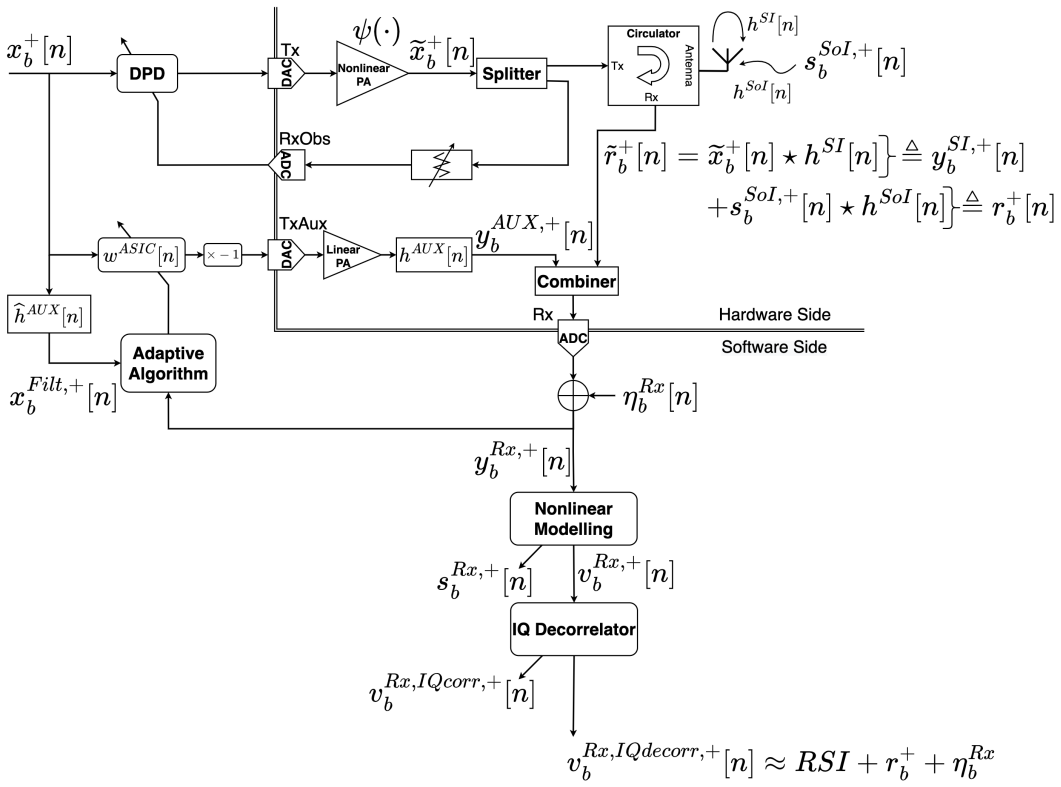

Figure 2.12: A diagram that shows linear ASIC, Nonlinear DSIC, and IQ Decorrelator signal processing blocks and hardware component in a complete picture.

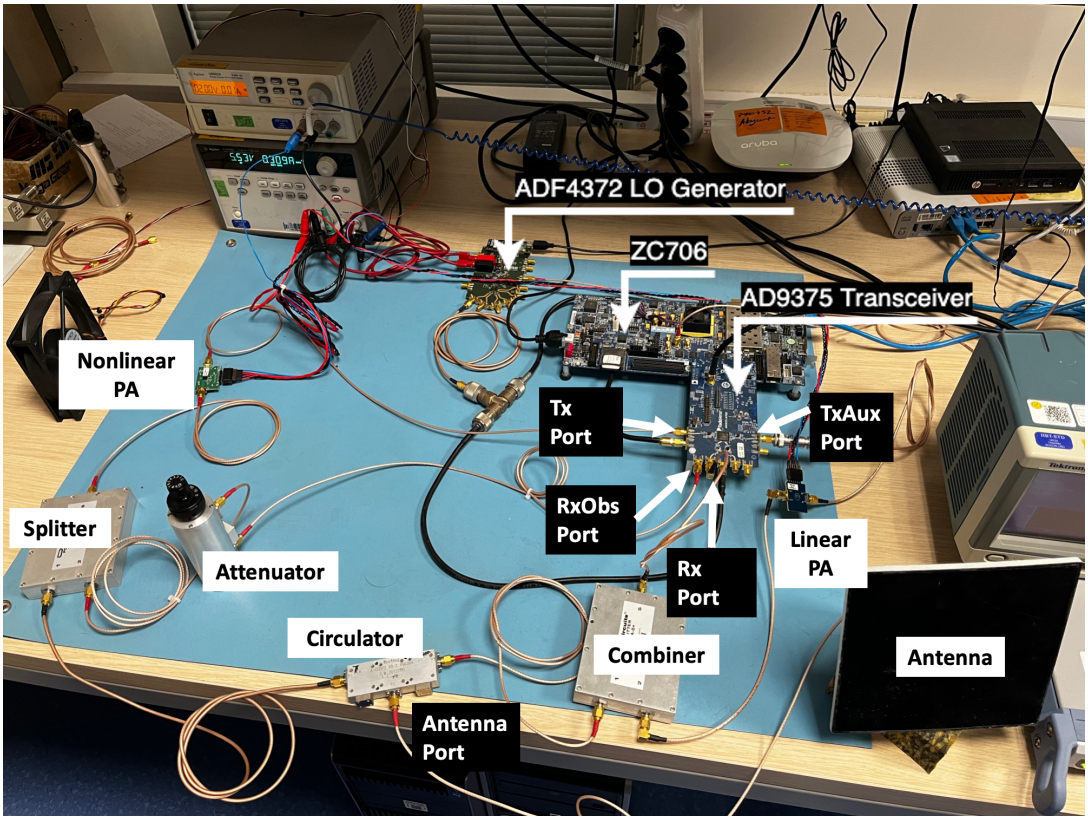

Figure 2.13: Nonlinear, single-antenna hardware setup and RF components.

to 2550 MHz and 122.88 Msps, respectively. Then, the predistorted transmit signal is sent from Tx Port to the high gain ($\approx$ 35 dB) nonlinear PA, SKY66397-12 [41]. The output of the nonlinear PA is splitted into two, $\widetilde{x}_b^+[n]$, and fed both into the circulator and the observation channel. On the way to the observation channel, the PA output is attenuated in order not to saturate the RxObs Port. On the way to the circulator and then to the Rx Port the PA output is suppressed $\approx$ 19-20 dB by the circulator and $\approx$ 4-5 dB by the combiner located prior to the Rx Port. The analog cancellation signal is sent from the TxAux Port to the low gain ($\approx$ 16 dB) linear power amplifier, SKY67189-396LF [42]. The output of the linear PA, $y_b^{AUX,+}[n]$, is then combined with the signals coming from the Antenna Port of the circulator, $\widetilde{r}_b^+[n]$. The antenna connected to the Antenna Port of the circulator is circularly polarized. Thus, the linear ASIC algorithm presented in Section 2.2 should deal with time-varying SI channel across batches, $h_{(i)}^{SI}[n]$. The equation (2.15) tracks the time-varying SI channel across batches while the SI channel that a single batch experiences, $h^{SI}[n]$, is assumed to be static. This assumption is related with a data capturing delay, t_{delay}, which is the time

passes between the starting sample of the consecutive batches and it stems from the hardware setup. The time duration of the batch $\left(\frac{\mu N^{sym} B}{fs} \approx 1.7 \text{ ms}\right)$ is much smaller than the data capturing delay $\left(t_{delay} \approx 2 \text{ s}\right)$ where $\mu N^{sym} = 8192$, $B = 25$.

In order to perform SIC, the DSP blocks shown in Figure 2.12 should be trained and filter coefficients should be determined first. Therefore, three operational modes are defined. These operational modes are introduced in the following section and the performance of the linear ASIC, nonlinear DSIC, and IQ Decorrelator algorithms is evaluated from PSD plots by using the same average antenna transmit power, $\approx$ 10 dBm, used in [11].

2.6 Operational Modes of the Hardware Setup

In Mode-0, the SoI is deactivated. First, fullband ($\approx$ 120 MHz) OFDM symbols are generated and transmitted from TxAux Port to the Rx Port to estimate the auxiliary channel, $\hat{h}^{AUX}[n]$, as presented in (2.9). Then, narrowband ($\approx$ 20 MHz[1]) OFDM symbols are generated to train the built-in DPD engine. The DPD activated and deactivated PSD plots is shown in Figure 2.14 and as it can be seen the circulator and the combiner suppresses the SI in propagation domain by $\approx$ 24 dB. It is important to note that the DPD training should be performed with the desired average nonlinear PA output power which corresponds to the desired average antenna transmit power. This mode is used only once, because the auxiliary channel, $h^{AUX}[n]$, is static and nonlinearity characteristics of the PA is stationary as it is cooled down with a fan in Figure 2.13.

In Mode-1, the SoI is continued to be deactivated and linear ASIC filter coefficients are trained through eight batches, as presented in (2.15). The effect of updating the ASIC filter coefficients is shown in the spectrum in Figure 2.15, where L^{Filt} =10 and $M = B = 25$. This mode is used when the SI channel, $h^{SI}[n]$ is changed drastically and the ASIC filter coefficients are required to be trained again. Thus, the frequency of using the Mode-1 depends on the environment that the IBFD radio operates.

[1]As the sampling rate of the ADRV9375 Evaluation Board is set to 122.88 Msps and a 20 MHz bandwidth signal is used, the estimated channel taps and ASIC&DSIC filter taps would become upsampled.

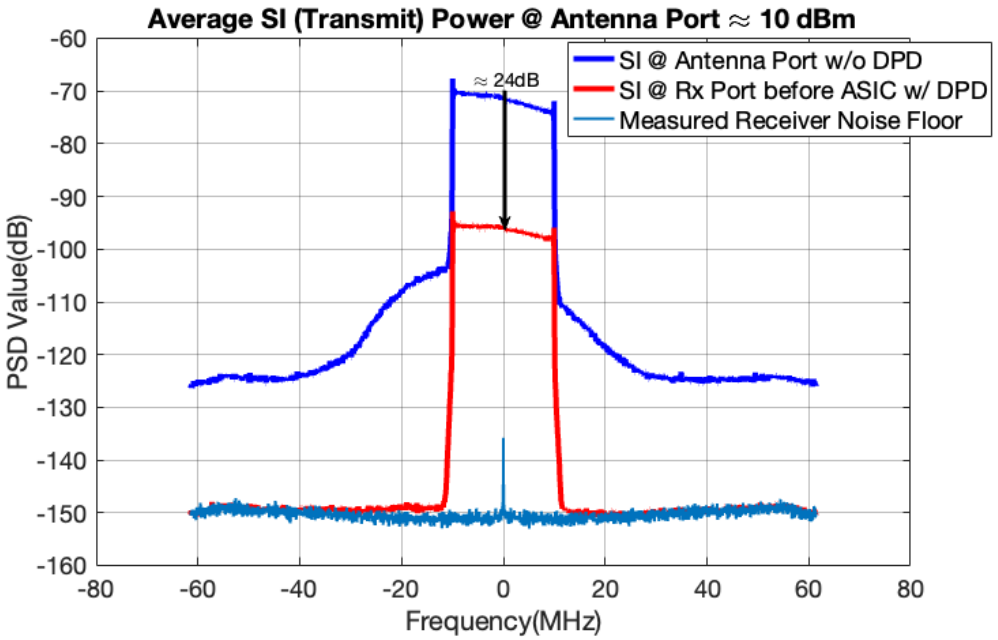

Figure 2.14: Mode-0. Difference between DPD activated and deactivated SI signals in the spectrum. The amount of propagation domain SIC by the circulator and the combiner should be read from the in-band as the blue spectrum is raised from the receiver noise floor by ≈ 24 dB.

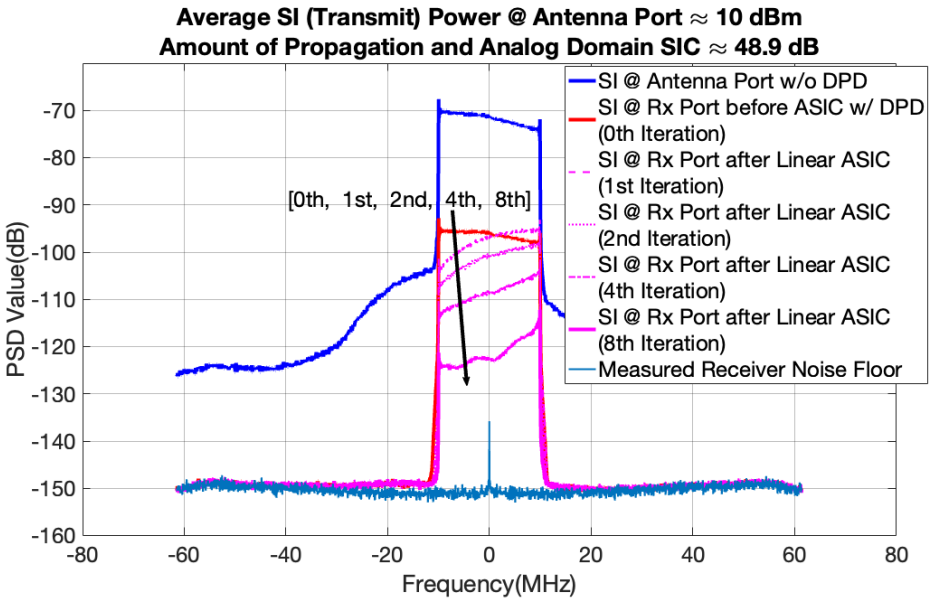

Figure 2.15: Mode-1. The received signal at Rx Port after ASIC iterations are shown in the spectrum progressively.

In Mode-2, linear ASIC is switched to testing phase and trained ASIC filter coefficients are used as it is shown in (2.11). SoI can be activated in this mode. However, PSD plots do not include SoI. SoI included analysis are in Chapter 5. Nonlinear DSIC and IQ Decorrelator filters are both trained as in (2.22) and (2.25), respectively. Then nonlinear DSIC and IQ Decorrelator filters are used as in (2.19) and (2.26), respectively. The results of nonlinear DSIC and IQ Decorrelator are shown in Figure 2.16, where $K^{GMP} = 5$, $L^{GMP} = 8$, $M^{GMP} = 2$, $L^{IQ} = 15$, and $M = B = 25$. The IBFD radio is in this mode of operation most of the time unless it is in the Mode-1 due to the saturation of the Rx Port because of the changing SI channel and the aging of the ASIC filter coefficients.

In conclusion, the previously proposed linear ASIC, nonlinear DSIC algorithms in [11] and recently proposed IQ Decorrelator algorithm result a P_{RSI} level that is close to the receiver noise floor, where the average antenna transmit power is $\approx$ 10 dBm. The receiver noise floor is measured by terminating the input ports of the combiner located prior to the Rx Port. In the next chapter, the algorithms are evaluated at higher average antenna transmit powers.

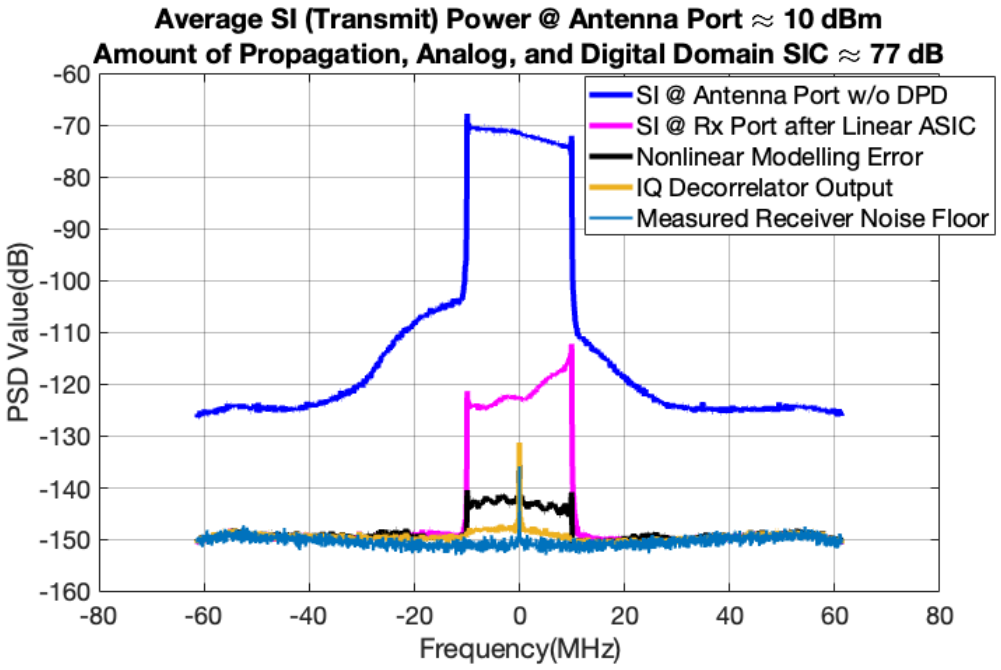

Figure 2.16: Mode-2. SIC summary in the spectrum after linear ASIC, nonlinear DSIC, and IQ Decorrelator.

CHAPTER 3

EVALUATION OF THE DISCUSSED SIC ALGORITHMS AT HIGHER AVERAGE ANTENNA TRANSMIT POWERS

In this chapter, the performance of the SIC algorithms discussed in Chapter 2 are evaluated with the same parameters in Sections 2.5 and 2.6 at higher average antenna transmit powers, $\approx$ 13 dBm and $\approx$ 16.5 dBm. After the evaluation, it is shown that the performance of the previously discussed SIC algorithms are limited. This limitation results in the discovery of the transmitter noise in the used hardware setup.

3.1 The Performance of Operational Modes at Higher Average Antenna Transmit Powers

In Mode-0, higher average antenna transmit powers correspond to higher average PA output powers and, thus, under strong nonlinearity the built-in DPD cannot linearize the PA completely, as presented in Figure 3.1.

In Mode-1, due to the existence of a nonlinearized PA, the performance of linear ASIC decreases and, more iterations are required to perform the same level of ASIC in the in-band, as shown in Figure 3.2.

In Mode-2, the performance of IQ Decorrelator starts to be less effective as the average antenna transmit power increases as presented in Figure 3.3.

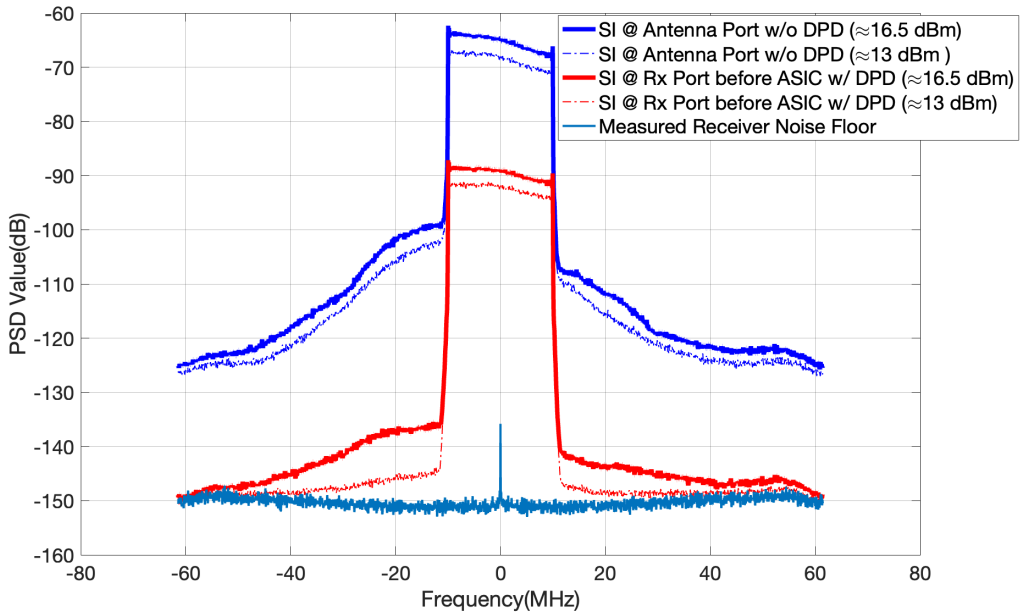

Figure 3.1: Mode-0. The performance of the built-in DPD, where average antenna transmit power $\approx$ 13 dBm and $\approx$ 16.5 dBm.

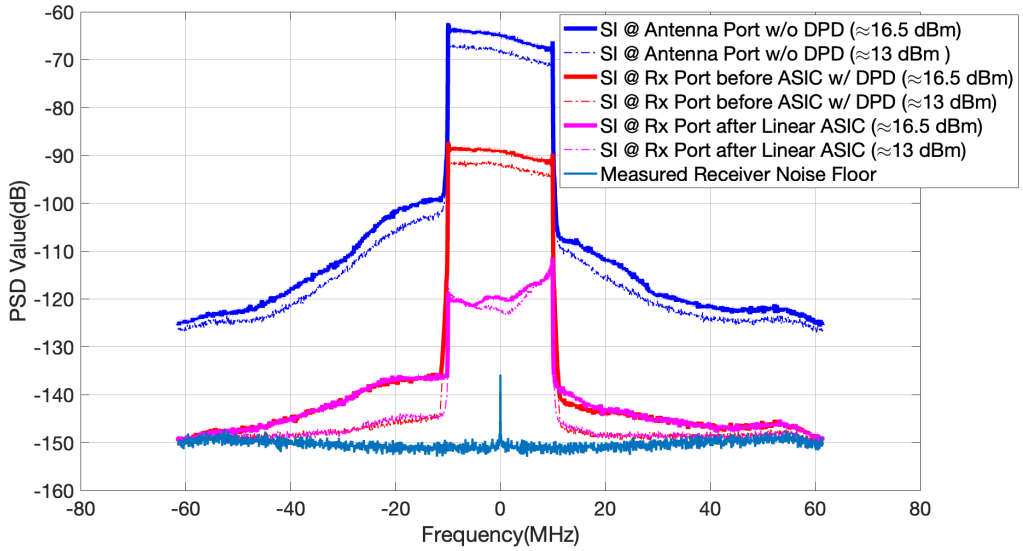

Figure 3.2: Mode-1. The performance of ASIC after iterations, where average antenna transmit power $\approx$ 13 dBm and $\approx$ 16.5 dBm. The amount of propagation and analog domain SIC is $\approx$ 51 dB for the former and $\approx$ 53 dB for the latter.

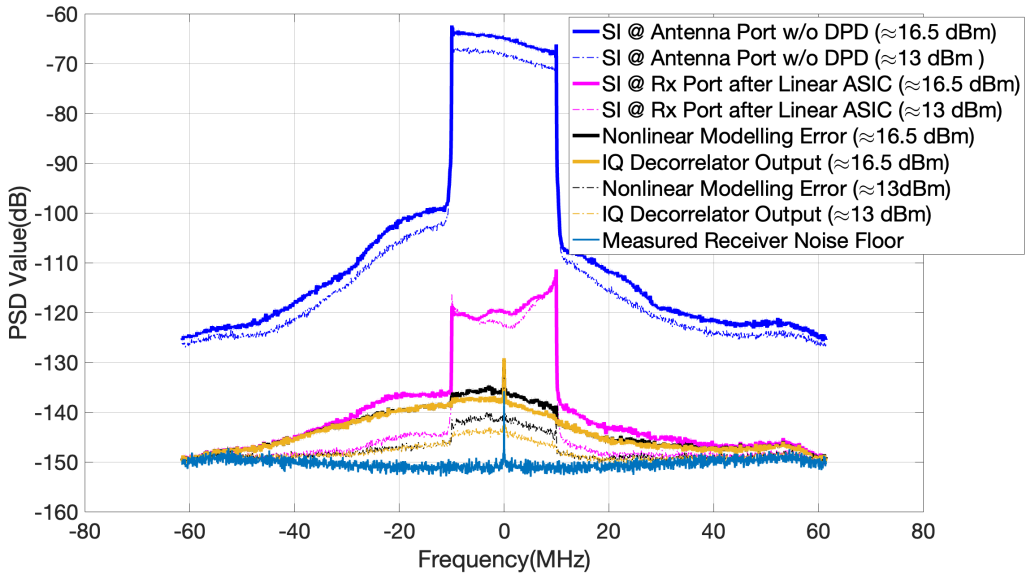

Figure 3.3: Mode-2. SIC summary in the spectrum after propagation, analog, and digital domains, where average antenna transmit power $\approx$ 13 dBm and $\approx$ 16.5 dBm. The amount of propagation, analog, and digital domain SIC is $\approx$ 76.5 dB for the former and $\approx$ 73 dB for the latter.

3.2 Discovery of the Transmitter Noise in the Nonlinear, Single-Antenna Hardware Setup

After the IQ Decorrelator, P_{RSI} levels in Figure 3.3 start to diverge from the receiver noise floor as the average antenna transmit power increases. The observed higher P_{RSI} level results in the discovery of transmitter noise due to the high average antenna transmit power. In the next chapter, the hardware setup is simulated in MATLAB with an addition of the transmitter noise in the synthetic environment and the limiting effect of the transmitter noise on the SIC algorithms is going to be shown. Then, a noise cancellation algorithm is going to be proposed which utilizes the observation receiver channel to capture the nonlinear PA output on the ordinary transmission chain. The noise cancellation algorithm exploits the observation and ordinary receiver channels containing the same transmitter noise realization. Finally, the hardware setup is used to evaluate the performance of the noise cancellation algorithm.

CHAPTER 4

DEVELOPMENT OF THE NOISE CANCELLATION ALGORITHM

In this chapter, the hardware setup presented in Section 2.5 is simulated in MATLAB from scratch with an addition of the transmitter noise in the ordinary channel and a PA Model instead of a DPD. After that the ASIC, nonlinear DSIC algorithms described in Sections 2.2 and 2.3 are applied to perform SIC, respectively. In the synthetic environment the IQ Decorrelator algorithm is not needed, as IQ Imbalance is not present. Then, high P_{RSI} level is going to be shown to identify the limiting effect of the transmitter noise on the SIC algorithms. Then, a transmitter noise cancellation algorithm is proposed in the synthetic environment by exploiting the fact that the observation and ordinary receiver channels contain the same transmitter noise realization. Lastly, the hardware setup is used to evaluate the performance of the noise cancellation algorithm. In this chapter, all performance evaluations are performed from the PSD plots, where the SoI is deactivated. SoI included analysis is presented in Chapter 5.

4.1 Performance of the Previously Proposed SIC algorithms in the Synthetic Environment containing Transmitter Noise

The synthetic environment containing transmitter noise is shown in Figure 4.1. Employed self-interference channel, $h^{SI}[n]$ and auxiliary channel, $h^{AUX}[n]$, are obtained from the hardware setup and total power of the channel taps is normalized to 0 dB as shown in Figure 4.2, where $n = -L^{Ch}, \cdots, L^{Ch}$ and $L^{Ch} = 30$. A 10 dB input backoff is applied to the transmitted signal, $x_b^+[n]$, and the SNR of the transmitted signal $E_b\left[|\mathbf{x}_b^+|^2\right]/\sigma_{Tx}^2$ is set to $\approx$ 50 dB by the additive white complex-valued transmitter noise, $\eta_b^{Tx}[n] \sim CN(0, \sigma_{Tx}^2)$. In the ordinary transmitter chain the nonlinear

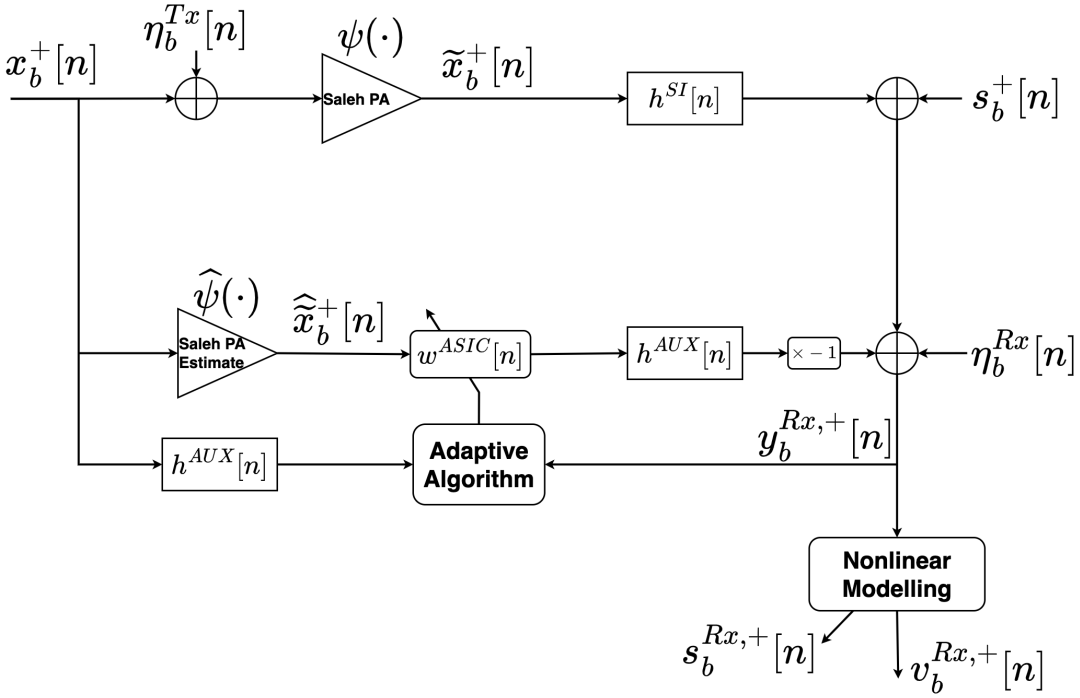

Figure 4.1: Diagram of the synthetic environment containing transmitter noise.

PA, $\psi(\cdot)$, is represented by Saleh Model with coefficients $\alpha_a = 2$, $\beta_a = 1$, $\alpha_\phi = \pi/4$, $\beta_\phi = 0.25$ [43]. With these coefficients and 10 dB input backoff, the PA applies on average $\approx$ 4.5 dB gain, as shown in Figure 4.3. The PA applies the gain both to the transmitted signal and the transmitter noise. Thus, the transmitter noise floor raises, as shown in Figure 4.4.

In Mode-0 the SNR of the PA output, $\widetilde{x}_b^+[n]$, is increased through integration and the nonlinear PA is modelled, $\widehat{\psi}(\cdot)$, by finding the GMP coefficients using the nonlinear DSIC algorithm in (2.22), where $K^{GMP} = 6$. The output of the PA estimate, $\widehat{\widetilde{x}}_b^+[n]$, is generated as it is shown in (2.19). The output of the PA and the output of the PA estimate are shown in the spectrum in Figure 4.5.

In Mode-1 ASIC filter coefficients are trained through a single batch as presented in (2.15), where $L^{Filt} = 10$, $\mu^{ss} = 0.95$, and $M = B = 25$. The received signal after ASIC, $y_b^{Rx,+}[n]$, is shown in the spectrum in Figure 4.6. It is known that the transmitter noise floor stands higher than the receiver noise floor, [2, 12, 15] and thus the receiver noise, $\eta_b^{Rx}[n] \sim CN(0, \sigma_{Rx}^2)$, is set to $\approx$ 20 dB below the transmitter

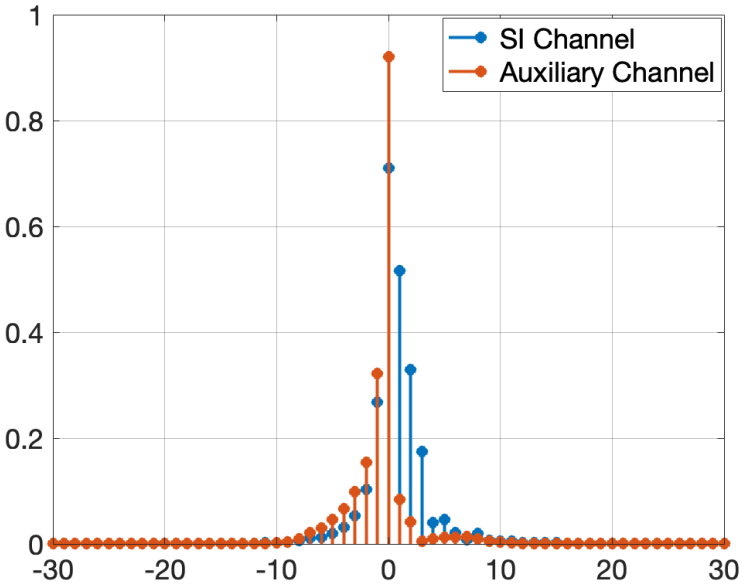

Figure 4.2: Estimated channel from the hardware setup.

noise. In other words, the receiver noise is ≈ 24.5 dB below the raised transmitter noise. An ideal IBFD system should utilize ASIC&DSIC algorithms such that the SI

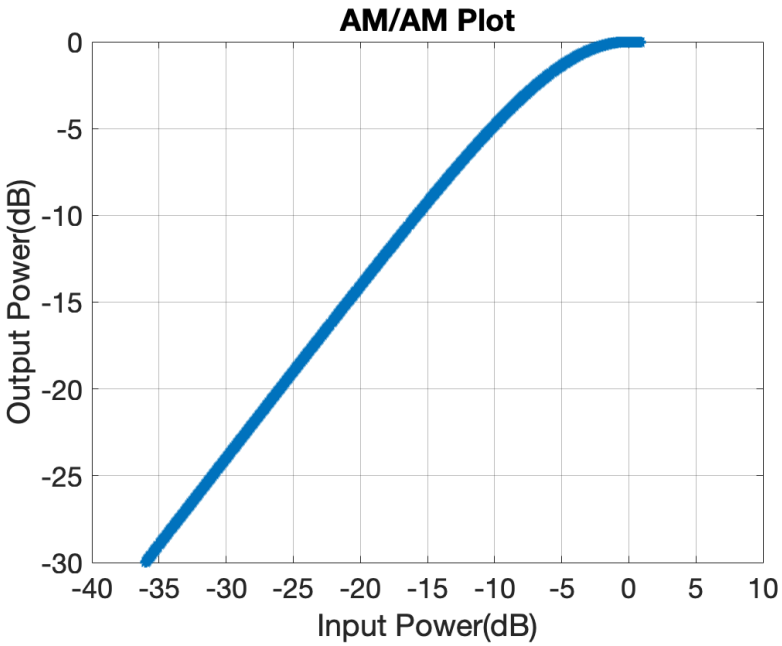

Figure 4.3: Input signal average power is ≈ -10 dB and input signal peak power is ≈ 0.8 dB.

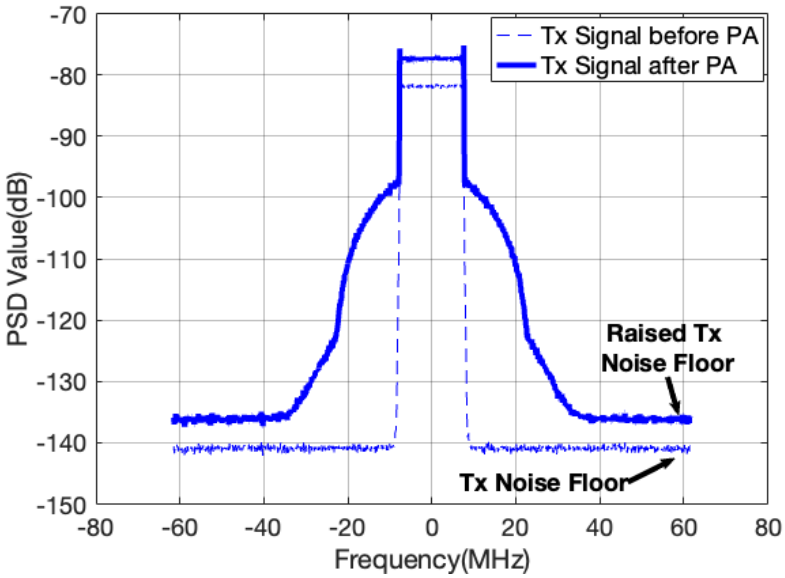

Figure 4.4: The effect of the PA on the transmitted signal in the spectrum.

is suppressed up to the receiver noise floor.

In Mode-2, ASIC is switched to testing phase and trained ASIC filter coefficients are

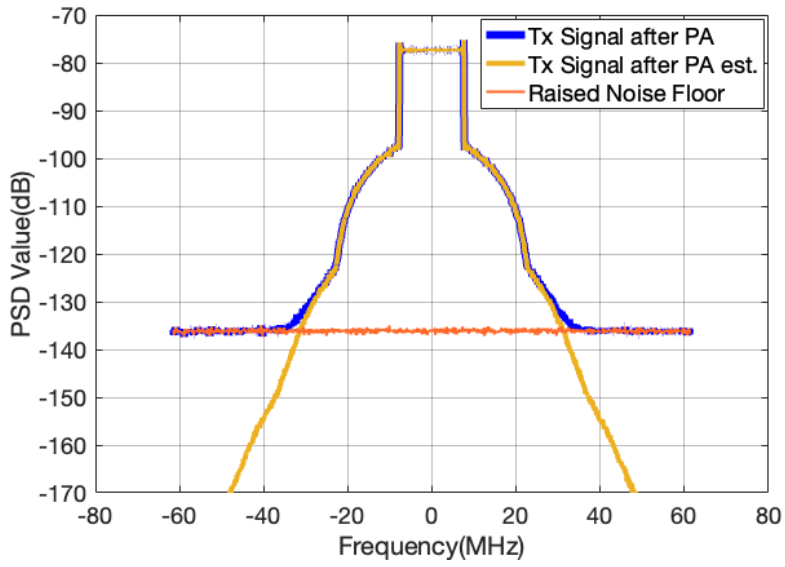

Figure 4.5: Mode-0. The outputs of the PA and PA estimate in the spectrum. The time domain mean squared error between the actual and estimated outputs is in the order of 1e-6.

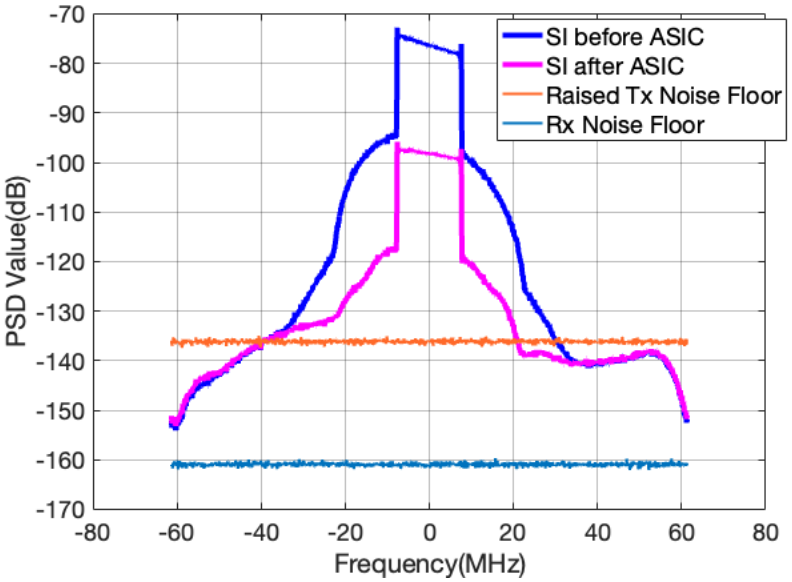

Figure 4.6: Mode-1. The performance of ASIC filter is limited as the step size, μ^{ss}, is set to 0.95 and not to 1. This is done on purpose in order to show the performance of the nonlinear DSIC algorithm in Mode-2.

used as it is shown in (2.11). Moreover, nonlinear DSIC filter is trained as it is shown in (2.22) and tested as it is shown in (2.19), where $K^{GMP} = 6$, $L^{GMP} = 30$, $M^{GMP} = 0$, and $M = B = 25$. SoI can be activated in this mode. However, PSD plots do not include SoI. SoI included analysis are in Chapter 5. When the SoI is deactivated the nonlinear modelling error, $v_b^{Rx,+}[n]$, is shown in the spectrum in Figure 4.7. As it can be seen, the P_{RSI} level is high and it is around the raised transmitter noise floor. Furthermore, when the transmitter noise is removed from the synthetic environment the SI can be cancelled up to the receiver noise floor, as it shown in Figure 4.8. Thus, it is observed that the existence of the transmitter noise in the synthetic environment results in a similar bottleneck on the SIC algorithms presented in Chapter 3.

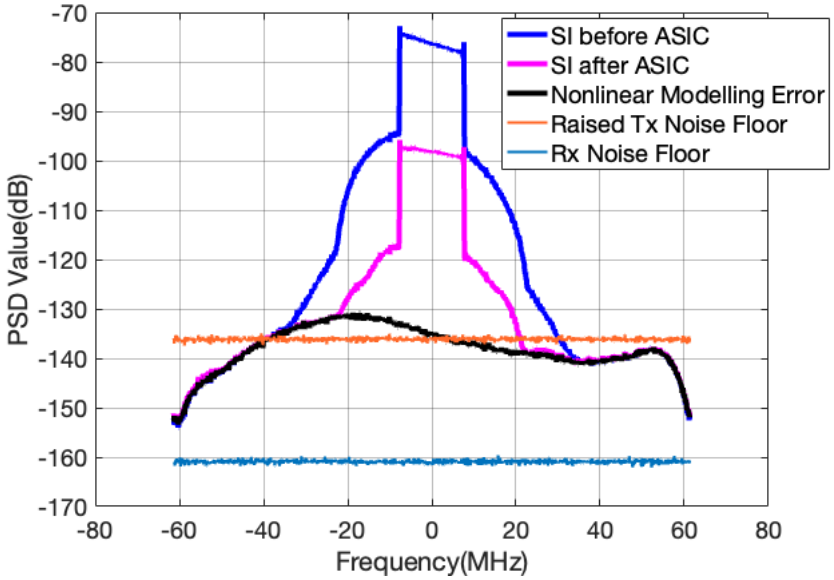

Figure 4.7: Mode-2. SIC summary in the spectrum after ASIC and nonlinear DSIC with transmitter noise.

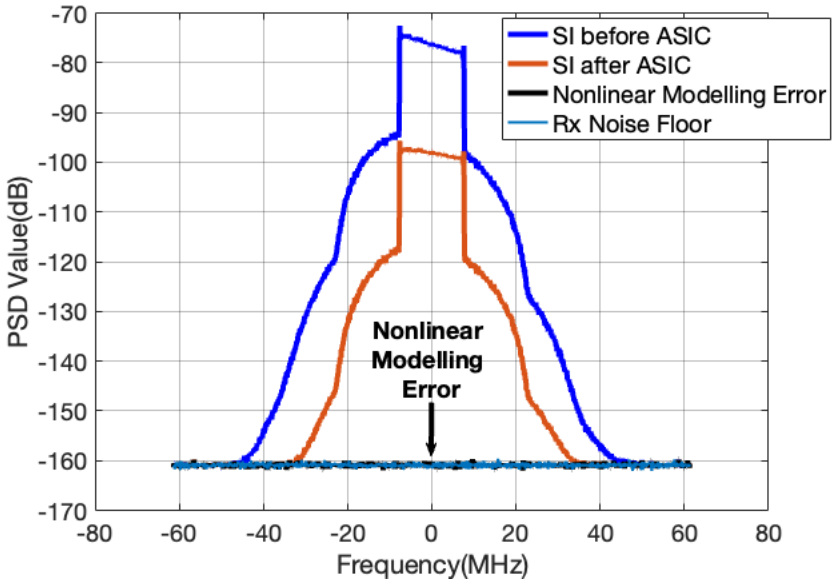

Figure 4.8: Mode-2. SIC summary in the spectrum after ASIC and nonlinear DSIC without transmitter noise.

4.2 Transmitter Noise Cancellation Algorithm and its Performance in the Synthetic Environment

In the hardware setup shown in Figure 2.12 and 2.13, the observation channel has already been used to train the DPD on the ordinary transmitter chain. In Mode-2, transmitter noise cancellation algorithm further utilizes the observation channel to capture the same transmitter noise realization that the ordinary receiver chain has been affected. The transmitter noise cancellation algorithm diagram in the synthetic environment is shown in Figure 4.9:

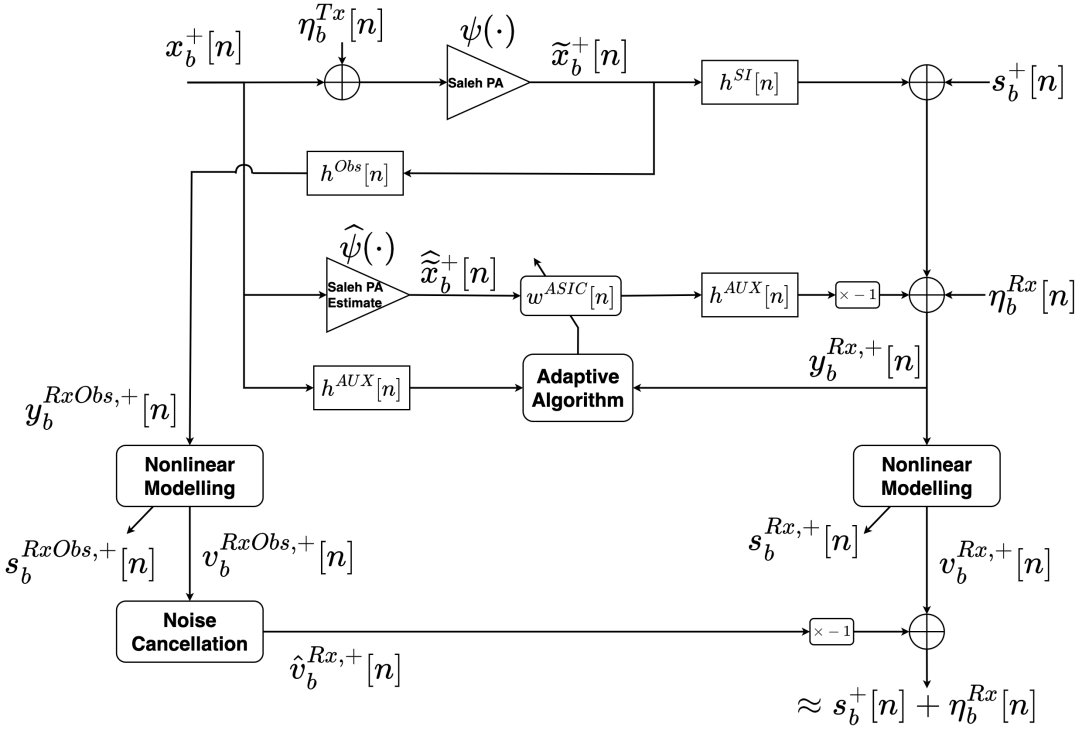

Figure 4.9: Diagram of the proposed noise cancellation algorithm in the synthetic environment containing transmitter noise.

The received signal from the observation channel, $y_b^{RxObs,+}[n]$, can be written as in (4.1):

$$y_b^{RxObs,+}[n] = \widetilde{x}_b^+[n] \star h^{Obs}[n]. \tag{4.1}$$

The PA output, $\widetilde{x}_b^+[n]$ can be written as in (4.2) to reveal the raised transmitter noise term, $\widetilde{\eta}_b^{Tx}[n]$:

$$\widetilde{x}_b^+[n] = \psi\big(x_b^+[n]\big) + \underbrace{\psi\big(x_b^+[n] + \eta_b^{Tx}[n]\big) - \psi\big(x_b^+[n]\big)}_{\triangleq \widetilde{\eta}_b^{Tx}[n]}. \tag{4.2}$$

In Figure 4.9, pictorial description of nonlinear modelling of the observation channel is shown. GMP basis functions can be used to model the $\mathbf{y}_b^{RxObs,+}$ to obtain the raised transmitter noise term as a nonlinear modelling error as it is shown in (4.3):

$$\mathbf{y}_b^{RxObs,+} = \underbrace{\mathbf{\Phi}(\mathbf{x}_b^+)\boldsymbol{\beta}^{RxObs}}_{\triangleq \mathbf{s}_b^{RxObs,+}} + \mathbf{v}_b^{RxObs,+}, \tag{4.3}$$

where $\boldsymbol{\beta}^{RxObs}$ is a vector containing GMP coefficients and $\mathbf{\Phi}(\mathbf{x}_b^+)$ is a matrix containing the GMP basis functions for $\mathbf{x}_b^+$ in its columns, and $\mathbf{v}_b^{RxObs,+}$ represents the modelling error. In the training phase of nonlinear modelling in Mode-2, CP&CS &Window-free M number of blocks (from the same batch) are used to minimize the Block-Averaged MSE via LS to find the GMP coefficients, $\boldsymbol{\beta}^{RxObs}$. Please refer to (4.4)-(4.6):

$$\frac{\partial E_b\Big\{\Big|\mathbf{v}_b^{RxObs}\Big|^2\Big\}}{\partial \boldsymbol{\beta}^{RxObs^H}} = \frac{\partial E_b\Big\{\big(\mathbf{y}_b^{RxObs^H} - \boldsymbol{\beta}^{RxObs^H}\mathbf{\Phi}(\mathbf{x}_b)^H\big)\big(\mathbf{y}_b^{RxObs} - \mathbf{\Phi}(\mathbf{x}_b)\boldsymbol{\beta}^{RxObs}\big)\Big\}}{\partial \boldsymbol{\beta}^{RxObs^H}}, \tag{4.4}$$

$$\begin{aligned} E_b\Big\{ -\mathbf{\Phi}(\mathbf{x}_b)^H\big(\mathbf{y}_b^{RxObs} - \mathbf{\Phi}(\mathbf{x}_b)\boldsymbol{\beta}^{RxObs}\big)\Big\} = \\ - E_b\Big\{\mathbf{\Phi}(\mathbf{x}_b)^H\mathbf{y}_b^{RxObs}\Big\} + E_b\Big\{\mathbf{\Phi}(\mathbf{x}_b)^H\mathbf{\Phi}(\mathbf{x}_b)\Big\}\boldsymbol{\beta}^{RxObs} \triangleq 0, \end{aligned} \tag{4.5}$$

$$\Rightarrow \boldsymbol{\beta}^{RxObs} = \left(\sum_{b=0}^{M-1}\mathbf{\Phi}(\mathbf{x}_b)^H\mathbf{\Phi}(\mathbf{x}_b)\right)^{-1}\left(\sum_{b=0}^{M-1}\mathbf{\Phi}(\mathbf{x}_b)^H\mathbf{y}_b^{RxObs}\right). \tag{4.6}$$

In (4.6) the matrix $\mathbf{\Phi}(\mathbf{x}_b)$ containing the GMP basis function for triplet (k,l,m) in its columns. The basis function is $x_b\big[n-l\big]\Big|x_b\big[n-l-m\big]\Big|^k$, where $k = 0,\cdots,K^{GMP}$ and $l = -L^{GMP},\cdots,L^{GMP}$ and $m = -M^{GMP},\cdots,M^{GMP}$. $\mathbf{\Phi}(\mathbf{x}_b)$ is of size

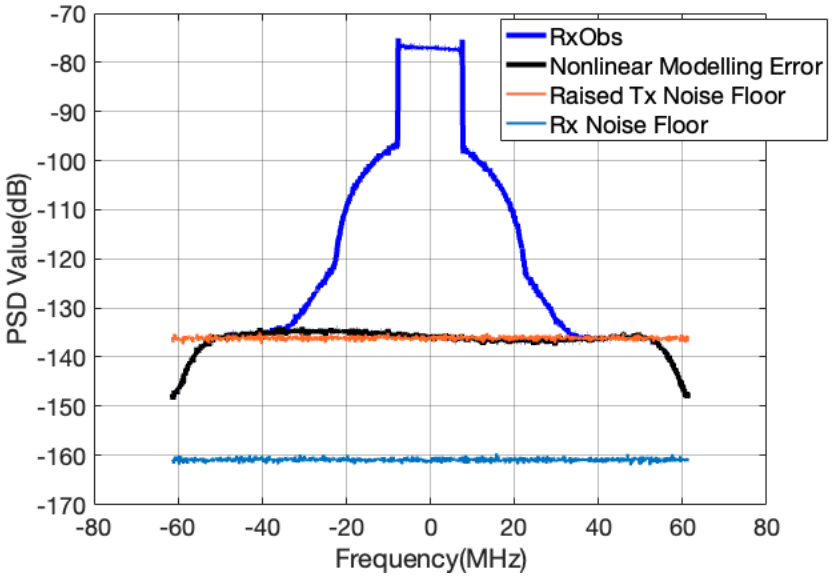

Figure 4.10: Mode-2. Performance of the nonlinear modelling on the observation channel in the spectrum.

$(\mu N^{sym} - 2L^{GMP} - 2M^{GMP}) \times (K^{GMP}(2L^{GMP}+1)(2M^{GMP}+1) + (2L^{GMP}+1))$, $\mathbf{y}_b^{RxObs}$ is of size $(\mu N^{sym} - 2L^{GMP} - 2M^{GMP}) \times 1$ and hence, $\boldsymbol{\beta}^{RxObs}$ becomes of size $(K^{GMP}(2L^{GMP}+1)(2M^{GMP}+1) + (2L^{GMP}+1)) \times 1$. In the testing phase of nonlinear modelling in Mode-2 shown in (4.3), $\boldsymbol{\Phi}(\mathbf{x}_b^+)$ is generated where the matrix is of size $(\mu N^{sym} + N^{CP} + N^{CS}) \times (K^{GMP}(2L^{GMP}+1)(2M^{GMP}+1) + (2L^{GMP}+1))$. Then, $\boldsymbol{\Phi}(\mathbf{x}_b^+)$ is used to generate $\mathbf{s}_b^{RxObs,+} = \boldsymbol{\Phi}(\mathbf{x}_b^+)\boldsymbol{\beta}^{RxObs}$ and the nonlinear modelling error becomes $\mathbf{v}_b^{RxObs,+} = \mathbf{y}_b^{RxObs,+} - \mathbf{s}_b^{RxObs,+}$.

When the parameters mentioned in Section 4.1 are used, the outputs of the nonlinear modelling, in Mode-2, can be estimated as shown in (4.7) and Figure 4.10:

$$\begin{aligned} s_b^{RxObs,+}[n] &\approx \psi\big(x_b^+[n]\big) \star h^{Obs}[n], \\ v_b^{RxObs,+}[n] &\approx \widetilde{\eta}_b^{Tx}[n] \star h^{Obs}[n]. \end{aligned} \tag{4.7}$$

The noise cancellation filter, $w^{NC}[n]$, uses $\mathbf{v}_b^{RxObs,+}$ to estimate $\mathbf{v}_b^{Rx,+}$ as both signals contain the same realization of the raised transmitter noise, where $n = -L^{NC}, \cdots, L^{NC}$. The error signal can be written as in (4.8):

$$\mathbf{e}_b^{+} \triangleq \mathbf{v}_b^{Rx,+} - \mathbf{V}_b^{RxObs,+}\mathbf{w}^{NC}, \tag{4.8}$$

where $\mathbf{V}_b^{RxObs,+}$ is a Toeplitz (convolution) matrix containing $\mathbf{v}_b^{RxObs,+}$ in its columns and $\mathbf{w}^{NC} = \Big[w^{NC}\big[-L^{NC}\big], \cdots, w^{NC}\big[L^{NC}\big]\Big]^T$. Minimization of the Block-Averaged MSE via LS reveals the $\mathbf{w}^{NC}$, as it is shown in (4.9)-(4.11). In the training phase of noise cancellation in Mode-2, CP&CS&Window-free M number of blocks (from the same batch) are used:

$$\frac{\partial E_b\Big\{\mathbf{e}_b^H\mathbf{e}_b\Big\}}{\partial \mathbf{w}^{NC^H}} = \frac{\partial E_b\Big\{\big(\mathbf{v}_b^{Rx^H} - \mathbf{w}^{NC^H}\mathbf{V}_b^{RxObs^H}\big)\big(\mathbf{v}_b^{Rx} - \mathbf{V}_b^{RxObs}\mathbf{w}^{NC}\big)\Big\}}{\partial \mathbf{w}^{NC^H}}, \tag{4.9}$$

$$\begin{aligned} E_b\Big\{ -\mathbf{V}_b^{RxObs^H}\big(\mathbf{v}_b^{Rx} - \mathbf{V}_b^{RxObs}\mathbf{w}^{NC}\big)\Big\} = \\ - E_b\Big\{\mathbf{V}_b^{RxObs^H}\mathbf{v}_b^{Rx}\Big\} + E_b\Big\{\mathbf{V}_b^{RxObs^H}\mathbf{V}_b^{RxObs}\Big\}\mathbf{w}^{NC} \triangleq 0, \end{aligned} \tag{4.10}$$

$$\Rightarrow \mathbf{w}^{NC} = \left(\sum_{b=0}^{M-1}\mathbf{V}_b^{RxObs^H}\mathbf{V}_b^{RxObs}\right)^{-1}\left(\sum_{b=0}^{M-1}\mathbf{V}_b^{RxObs^H}\mathbf{v}_b^{Rx}\right). \tag{4.11}$$

In (4.11) $\mathbf{V}_b^{RxObs}$ is a Toeplitz matrix (containing $\mathbf{v}_b^{RxObs}$ in its columns) of size $(\mu N^{sym} - 2L^{NC}) \times (2L^{NC}+1)$, $\mathbf{v}_b^{Rx}$ is of size $(\mu N^{sym} - 2L^{NC}) \times 1$, and thus $\mathbf{w}^{NC}$ is of size $(2L^{NC}+1)\times 1$. In the testing phase of noise cancellation in Mode-2 shown in (4.8), $\mathbf{V}_b^{RxObs,+}$ is generated where the matrix is of size $(\mu N^{sym} + N^{CP} + N^{CS}) \times (2L^{NC}+1)$.

When the parameters mentioned in Section 4.1 alongside with $L^{NC} = 30$ are used, the performance of the noise cancellation algorithm in the synthetic environment is shown in Figure 4.11. To conclude, the proposed algorithm can cancel the transmitter noise up to the receiver noise floor in the synthetic environment.

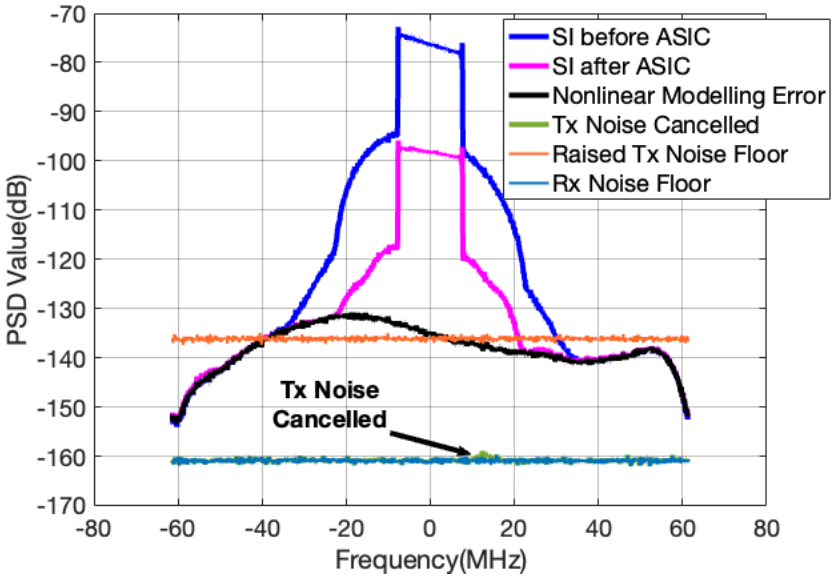

Figure 4.11: Mode-2. SIC summary in the spectrum after ASIC, nonlinear DSIC and noise cancellation.

4.3 Transmitter Noise Cancellation Algorithm and its Performance in the Hardware Setup

The noise cancellation algorithm proposed in Section 4.2[1] should be modified notation wise for the hardware setup as the system is a direct conversion system. An IQ Decorrelator signal processing block has to be inserted between the Nonlinear Modelling and Noise Cancellation signal processing blocks in the observation receiver chain shown in Figure 4.9. The modified diagram that shows linear ASIC, Nonlinear DSIC, IQ Decorrelator, and Noise Cancellation signal processing blocks and hardware components is shown in Figure 4.12.

IQ Decorrelator coefficients, $w_I^{RxObs}[n]$ and $w_Q^{RxObs}[n]$, are found as shown in (4.12) in the training phase of Mode-2. The details of the training phase and sizes of the vectors and matrices are previously discussed in Section 2.4 for the IQ Decorrelator in the ordinary receiver chain. Thus, only notation-wise modifications are done in

[1]The proposed noise cancellation algorithm is in fact based on Bussgang Decomposition where cross correlation of two Gaussian processes is equal to scaled cross correlation of processes plus uncorrelated distortion when either one of the process is affected by a nonlinearity. In Chapter 6, an alternative neural network aided noise cancellation algorithm is stated as a future work.

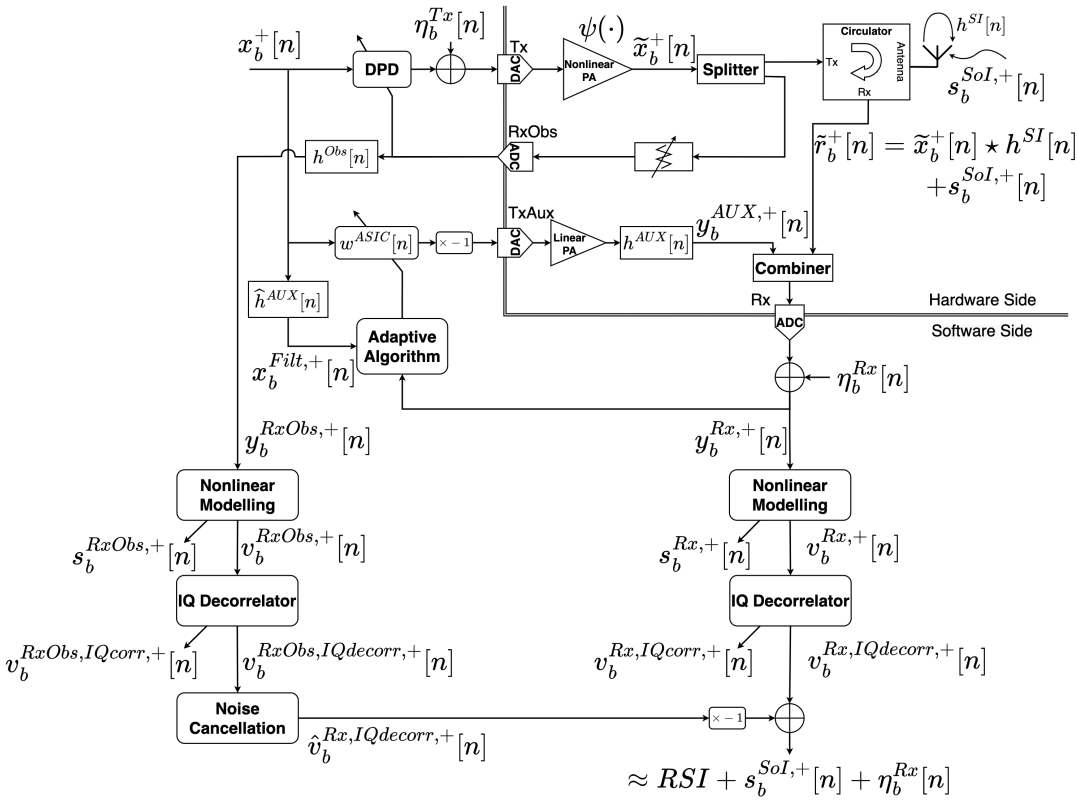

Figure 4.12: A complete diagram for pictorially describing the used hardware setup and utilized algorithms to perform transmitter noise aware SIC.

(4.12):

$$\begin{aligned}\mathbf{w}_I^{RxObs} &= \left(\sum_{b=0}^{M-1}\mathbf{A}_b^T\mathbf{A}_b\right)^{-1}\left(\sum_{b=0}^{M-1}\mathbf{A}_b^T Re\{\mathbf{v}_b^{RxObs}\}\right).\\ \mathbf{w}_Q^{RxObs} &= \left(\sum_{b=0}^{M-1}\mathbf{A}_b^T\mathbf{A}_b\right)^{-1}\left(\sum_{b=0}^{M-1}\mathbf{A}_b^T Im\{\mathbf{v}_b^{RxObs}\}\right).\end{aligned} \tag{4.12}$$

In the testing phase of Mode-2, the outputs of the IQ Decorrelator in observation chain shown in Figure 4.12 can be written as in (4.13):

$$\begin{aligned}\mathbf{v}_b^{RxObs,IQcorr,+} &= \mathbf{A}_b^+\mathbf{w}_I^{RxObs} + j\mathbf{A}_b^+\mathbf{w}_Q^{RxObs},\\ \mathbf{v}_b^{RxObs,IQdecorr,+} &= \mathbf{v}_b^{RxObs,+} - \mathbf{v}_b^{RxObs,IQcorr,+}.\end{aligned} \tag{4.13}$$

After the insertion of the IQ Decorrelator filter between the Nonlinear Modelling and Noise Cancellation blocks in the observation receiver chain, the proposed noise cancellation algorithm should use $\mathbf{v}_b^{RxObs,IQdecorr,+}$ to estimate $\mathbf{v}_b^{Rx,IQdecorr,+}$ as both signals contain the same realization of the raised transmitter noise. Then, in the training phase of Mode-2 the noise cancellation filter coefficients are found as it is shown in (4.14). The details of the training phase and sizes of the vectors and matrices are previously discussed in Section 4.2 for the noise cancellation block. Thus, only notation wise modifications are done in (4.14):

$$\mathbf{w}^{NC} = \left(\sum_{b=0}^{M-1} \mathbf{V}_b^{RxObs,IQdecorr^H} \mathbf{V}_b^{RxObs,IQdecorr} \right)^{-1} \left(\sum_{b=0}^{M-1} \mathbf{V}_b^{RxObs,IQdecorr^H} \mathbf{v}_b^{Rx,IQdecorr} \right). \quad (4.14)$$

In the testing phase of Mode-2, the output of the noise cancellation algorithm can be generated and subtracted from the IQ Decorrelator output of the ordinary receiver chain as shown in (4.15):

$$\mathbf{v}_b^{Rx,IQdecorr,+} - \mathbf{V}_b^{RxObs,IQdecorr,+} \mathbf{w}^{NC} \approx RSI + \mathbf{s}_b^{SoI,+} + \eta_b^{Rx}. \quad (4.15)$$

When the SoI is deactivated, performances of the SIC algorithms can be evaluated from Figures 4.13, 4.14, and 4.15. The proposed noise cancellation algorithm significantly improves the SIC performance at higher average antenna transmit powers, $\approx$ 13 dBm and $\approx$ 16.5 dBm. However, especially in the latter case, some RSI is left both in the in-band and out-of-band spectrum. This indicates an insufficiency in nonlinear modelling. More details will be given on that in Chapter 5 and Chapter 6. In the next chapter the SoI will be activated after the nonlinear DSIC, IQ Decorrelator, and Noise Cancellation filter coefficients are determined and the performance of each SIC algorithm is evaluated, separately, by calculating their BER versus SoI-SNR performance.

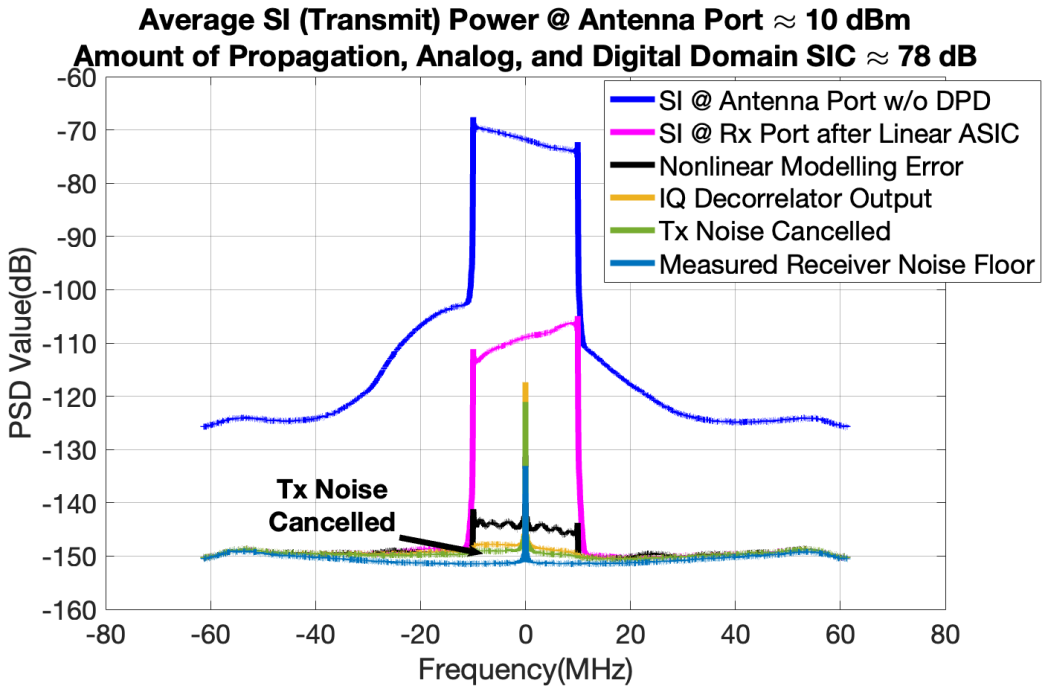

Figure 4.13: Mode-2. SIC Summary in the spectrum after linear ASIC, nonlinear DSIC, IQ Decorrelator, and Noise Cancellation where the average antenna transmit power is $\approx$ 10 dBm.

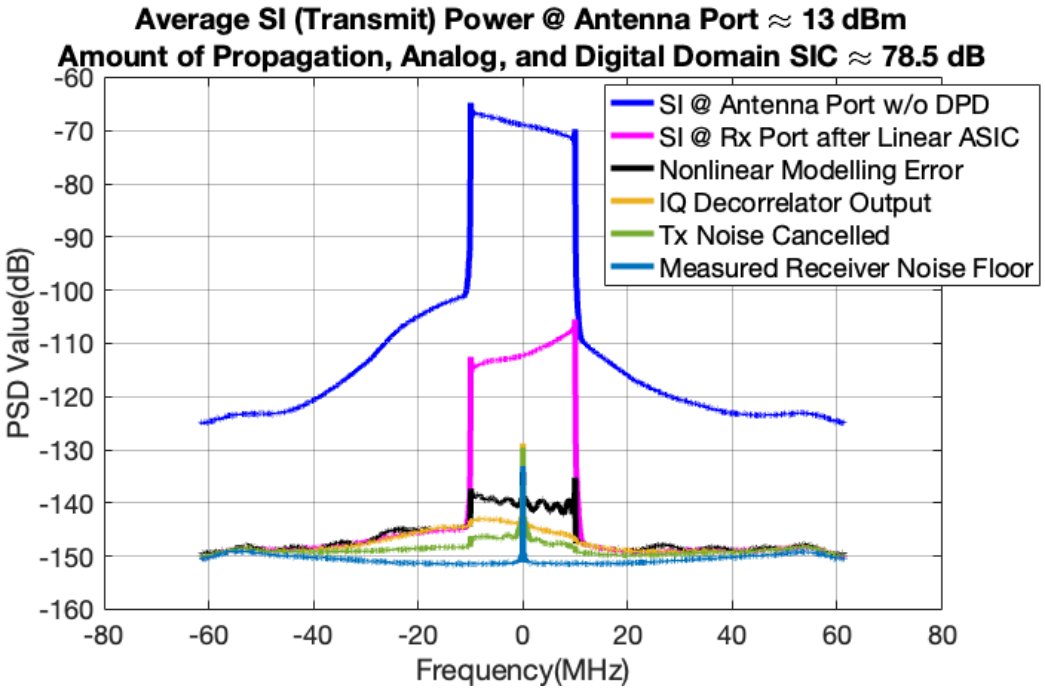

Figure 4.14: Mode-2. SIC Summary in the spectrum after linear ASIC, nonlinear DSIC, IQ Decorrelator, and Noise Cancellation where the average antenna transmit power is $\approx$ 13 dBm.

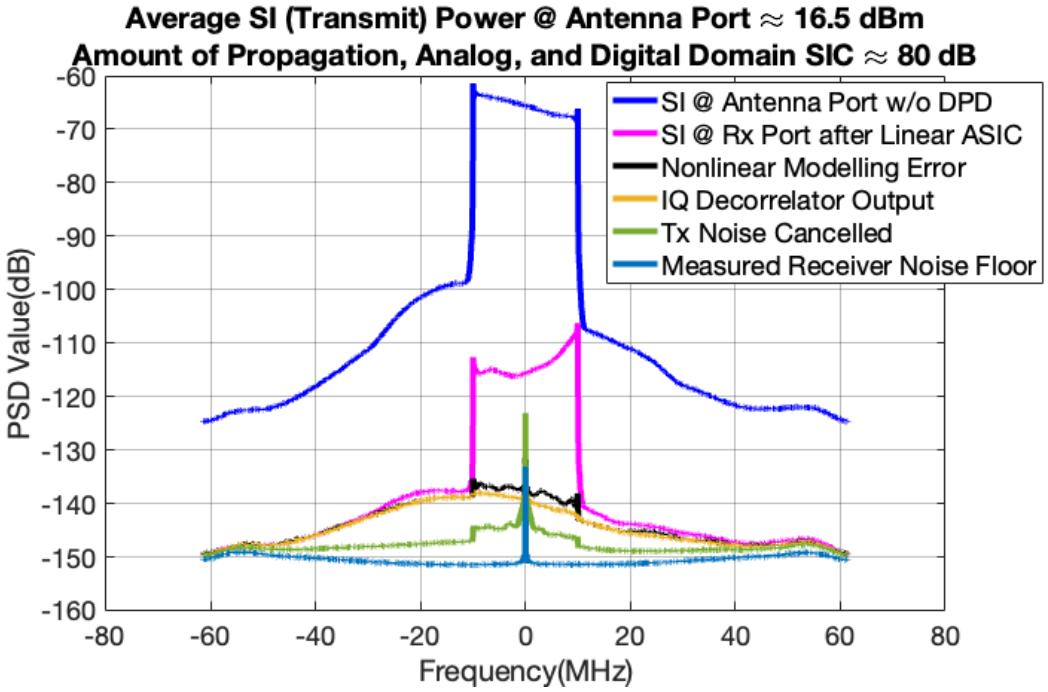

Figure 4.15: Mode-2. SIC Summary in the spectrum after linear ASIC, nonlinear DSIC, IQ Decorrelator, and Noise Cancellation where the average antenna transmit power is $\approx$ 16.5 dBm.

CHAPTER 5

NUMERICAL RESULTS

In this chapter, two types of SoI are inserted into the ASIC output after the coefficients of ASIC and DSIC filters are determined: In-Band SoI and Adjacent-Band SoI. In the In-Band SoI case, the SI and SoI overlap in the frequency domain. They occupy the same frequency band. In the Adjacent-SoI case, however, the SI and SoI occupy adjacent bands. Such a spectrum utilization does not violate the advantage of IBFD over HD on spectral efficiency. That is because the utilized adjacent band could have not been used due to the sidebands of the SI signal, otherwise. After the SoI insertion, the performance of SIC algorithms on demodulation of SoI is evaluated by BER versus SoI-SNR plots. In the IBFD system 16QAM modulation scheme is used and its performance is compared with a 256QAM hypothetical HD system, as it is the $2\times$ throughput counterpart. In the hypothetical HD system out-of-band radiation of other users and direct conversion related in-band contamination are neglected.

In Mode-0, the DPD is activated. After that, in Mode-1, the linear ASIC filter coefficients are trained and ASIC is performed in the testing phase of ASIC. The SoI is deactivated in Mode-0 and Mode-1. In Mode-2, the SoI is partially activated. For each $B = 400$ OFDM symbols long batch a $M = 25$ OFDM symbols long SoI-free period is used to train nonlinear DSIC, IQ Decorrelator and Noise Cancellation filters. The rest of the batch (375 OFDM symbols) contains SoI, as it is shown in Figure 5.1. To sum up, ASIC & DSIC filter coefficients are trained without SoI contamination and the IBFD achieves $\approx 1.93\times$ throughput compared to a 16QAM HD system, where it is assumed that Mode-0 and Mode-1 are rarely selected and the training duration of DSIC filters are neglected.

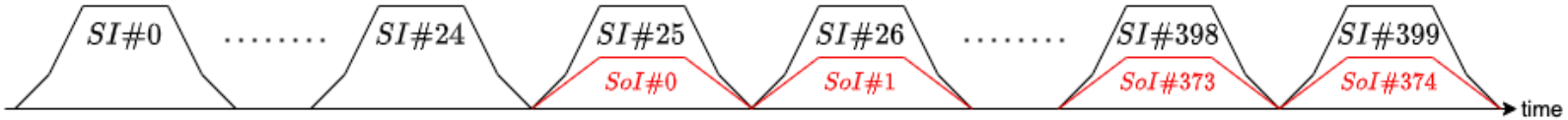

Figure 5.1: SI and SoI OFDM symbol structure in Mode-2 for BER measurement of SoI demodulation.

5.1 BER Performance of the In-Band SoI

For $\approx$ 10 dBm average antenna transmit power, the Noise Cancellation algorithm is cancelled the SI and the transmitter noise close to ($\sim$ 2 dB) the measured receiver noise floor, as it was shown in Figure 4.13 previously. When the In-Band SoI is activated the residual $\sim$ 2 dB performance gap becomes more observable, as it is shown in Figure 5.2. In fact, the same performance gap can be observed from the BER versus SoI-SNR plot in Figure 5.3. Furthermore, it can be seen from Figure 5.3 that for $\approx$ 10 dBm average antenna transmit power using only Nonlinear Modelling results a better BER performance across all SoI-SNRs than throughput-equivalent 256QAM HD system. In addition, even though IQ Decorrelator significantly improves the BER performance, the improvement that the Noise Cancellation introduces over IQ Decorrelator is limited.

For $\approx$ 13 dBm average antenna transmit power, the Nonlinear Modelling becomes insufficient to operate the IBFD system, as it is shown in Figure 5.4. In other words,

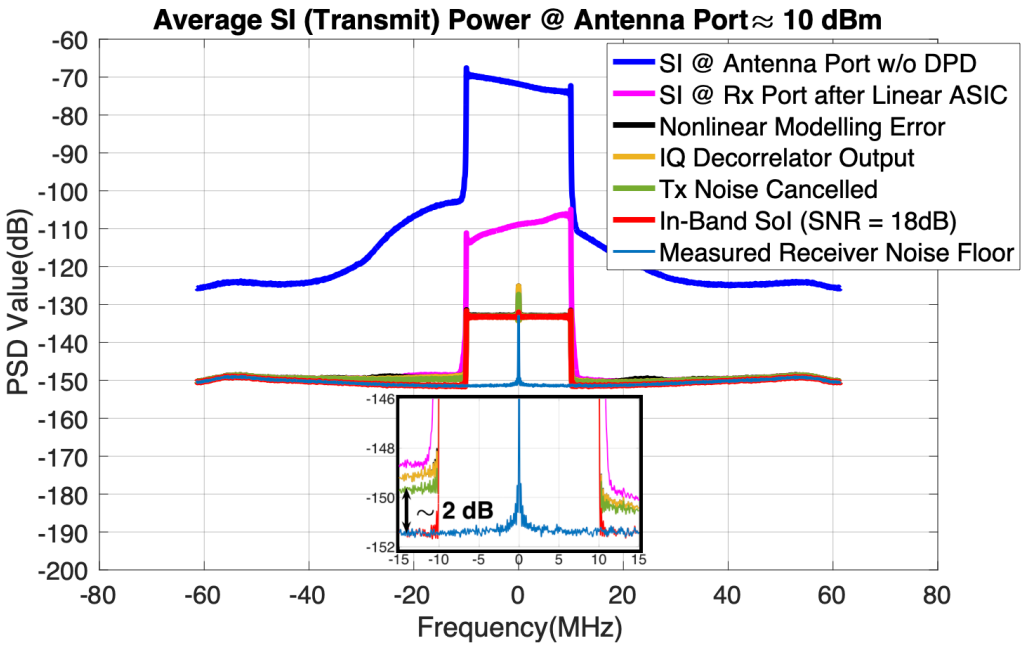

Figure 5.2: In-Band SoI is activated and SoI-SNR is set to 18 dB. SIC Summary in the spectrum after linear ASIC, nonlinear DSIC, IQ Decorrelator, and Noise Cancellation where the average antenna transmit power is $\approx$ 10 dBm.

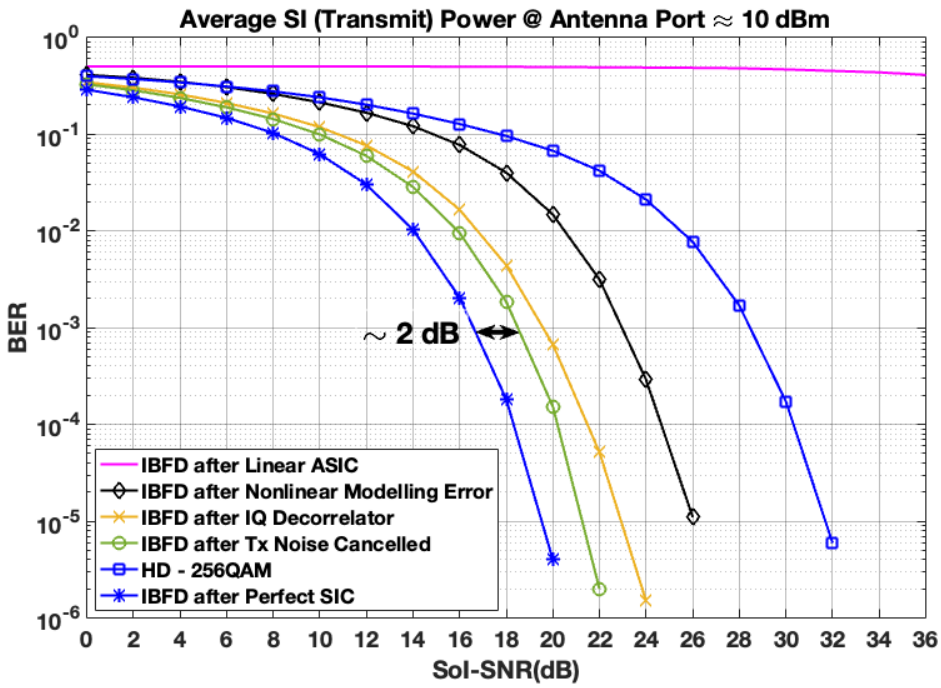

Figure 5.3: BER performance of the SIC algorithms for various In-Band SoI SNRs, where the average antenna transmit power is $\approx$ 10 dBm.

employing the 256QAM HD communication appears to be more favorable than using the 16QAM IBFD system, as the computational complexity of an IBFD system is much higher than the HD system. After the IQ Decorrelator and, especially, after the Noise Cancellation the 16QAM IBFD system becomes more favorable as it achieves the same BER performance by a $\sim$ 7 dB lower SoI-SNR than the 256QAM HD system.

For $\approx$ 16.5 dBm average antenna transmit power, the IQ Decorrelator becomes insufficient to operate the 16QAM IBFD system, as it is shown in Figure 5.5. At this point, if there is no observation channel in the IBFD hardware setup or if the proposed Noise Cancellation algorithm cannot be utilized, it is beneficial to employ a 256QAM HD system and eliminate the SIC algorithm burden. On the other hand, if the Noise Cancellation algorithm is utilized, it is possible to operate the 16QAM IBFD system, achieve $\sim 1.93\times$ throughput than the 16QAM HD system, and exploit MAC layer advantages such as prevention of hidden terminal and enhancement in fairness [8–10]. The Noise Cancellation algorithm is cancelled the SI and the transmitter noise to a

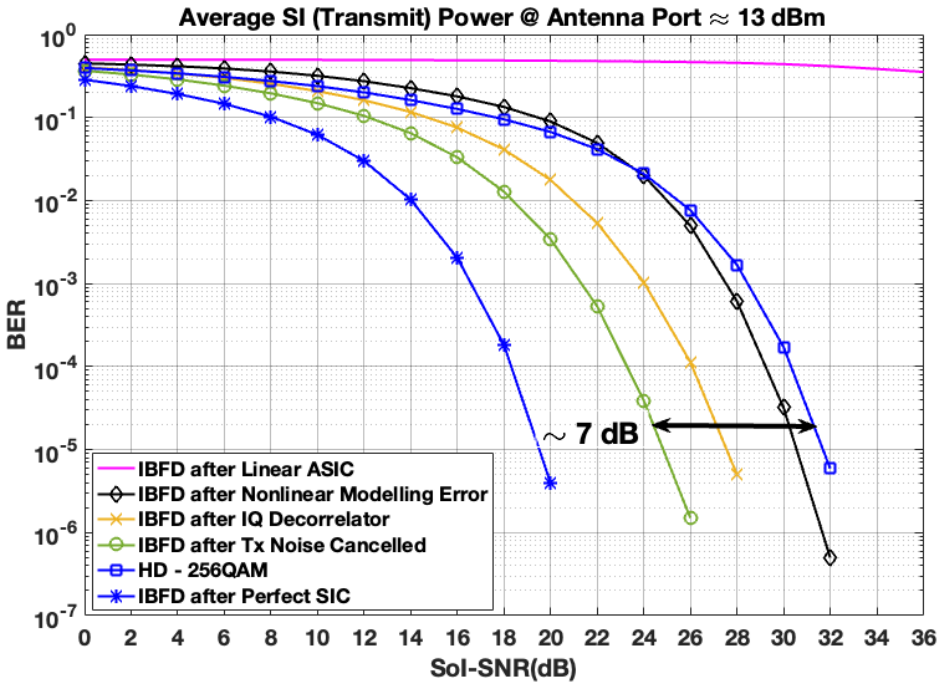

Figure 5.4: BER performance of the SIC algorithms for various In-Band SoI SNRs, where the average antenna transmit power is ≈ 13 dBm.

P_{RSI} that is ∼ 8 dB higher than the measured noise floor. The RSI left both in-band and out-of-band spectrum is shown in Figure 5.6. As mentioned in Chapter 4, such a RSI indicates an insufficiency in nonlinear modelling. How to improve the nonlinear modelling is touched upon in Chapter 6.

In Figure 5.7, SIC performance on the In-Band SoI demodulation for ≈ 10 dBm (pentagram marker & solid line), ≈ 13 dBm (circle marker & dashed line), and ≈ 16.5 dBm (diamond marker & dotted line) average antenna transmit powers are compared in the same plot. It is clearly shown that the proposed Noise Cancellation algorithm makes the 16QAM IBFD system more favorable than the throughput-equivalent 256QAM HD system for all the average antenna transmit powers that the used hardware setup supports.

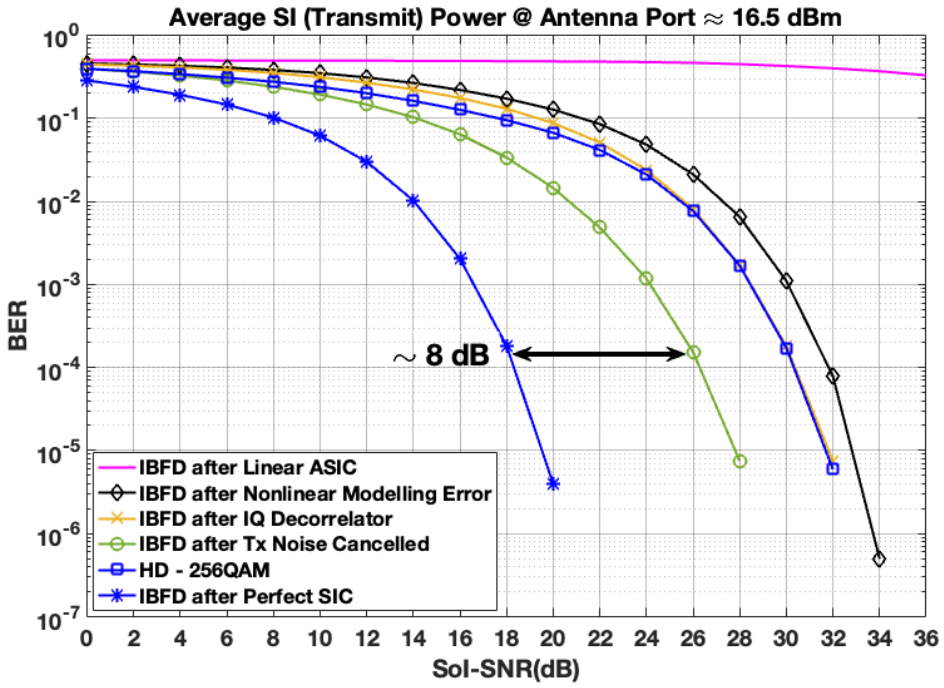

Figure 5.5: BER performance of the SIC algorithms for various In-Band SoI SNRs, where the average antenna transmit power is ≈ 16.5 dBm.

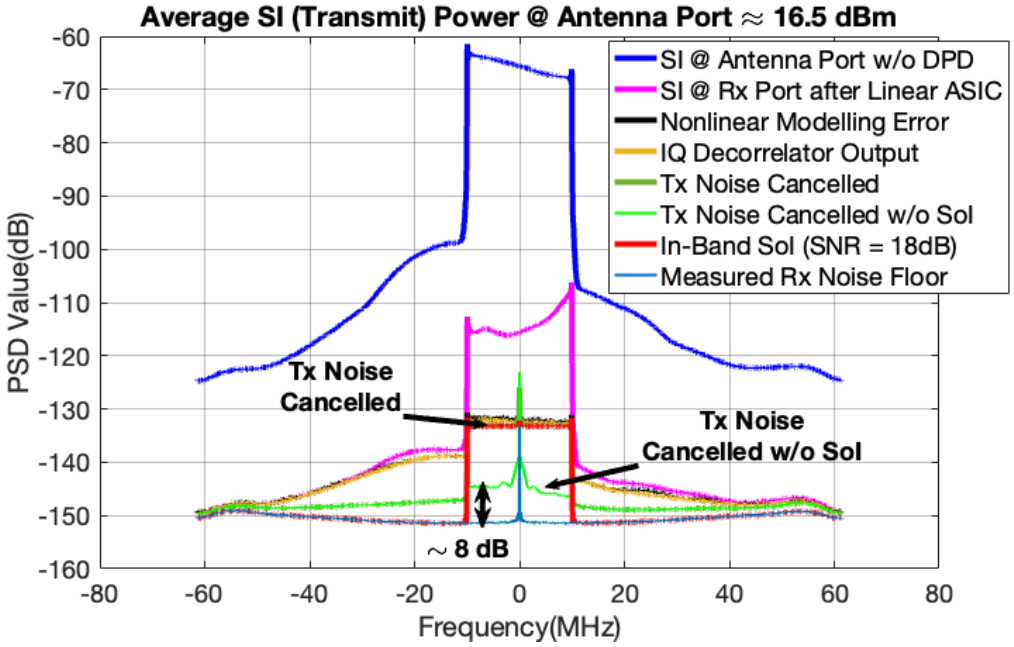

Figure 5.6: In-Band SoI is activated and SoI-SNR is set to 18 dB. SIC Summary in the spectrum after linear ASIC, nonlinear DSIC, IQ Decorrelator, and Noise Cancellation where the average antenna transmit power is ≈ 16.5 dBm.

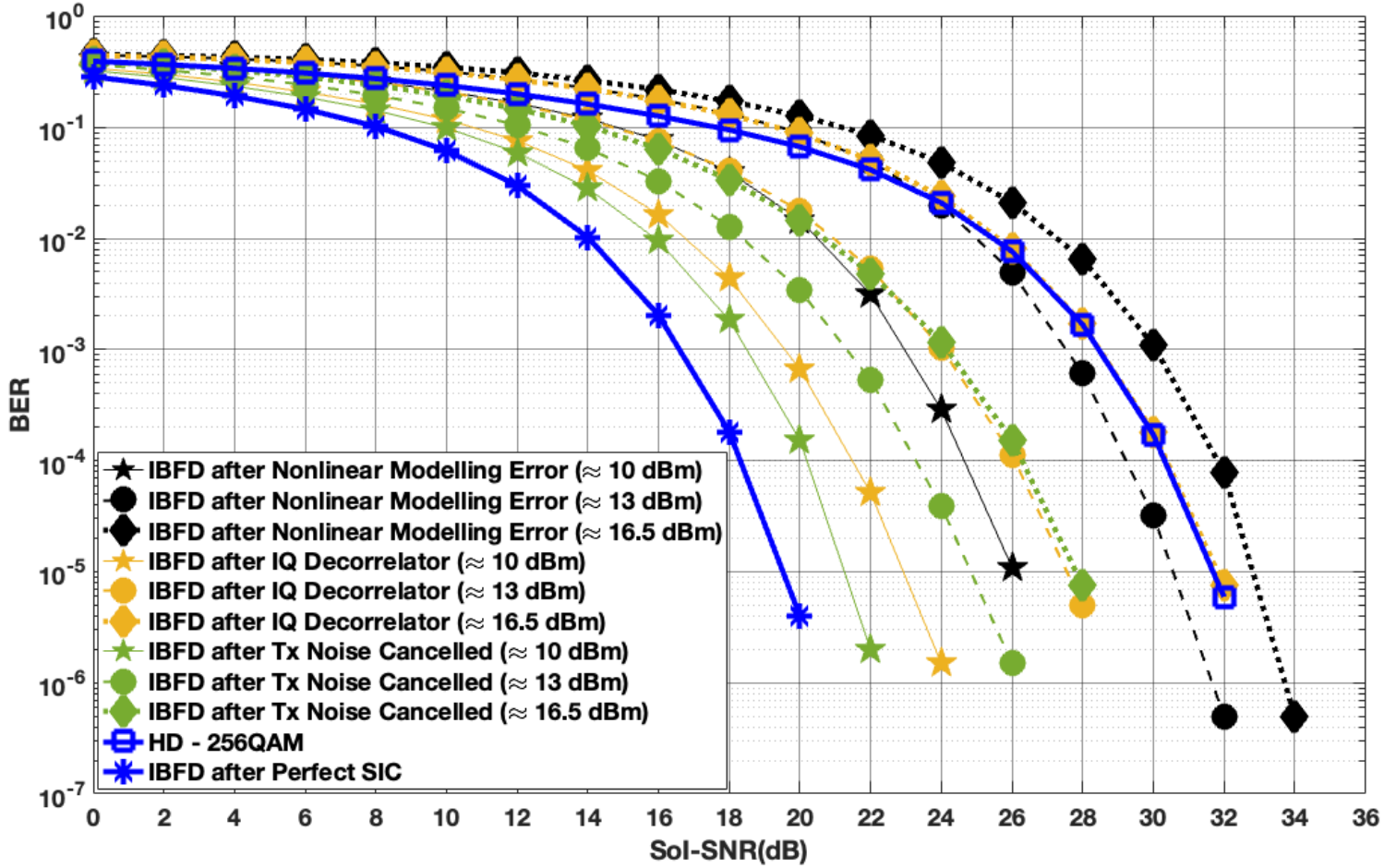

Figure 5.7: BER comparison of SIC algorithms operating in different average antenna transmit powers for various In-Band SoI SNRs.

5.2 BER Performance of the Adjacent-Band SoI

The Adjacent-Band SoI occupies a different band that the SI does, it is shifted by 20 MHz to the right in the spectrum, as it is shown in Figure 5.8. Thus, as the carrier frequency of the SI is set to 2550 MHz, the carrier frequency of the SoI is assumed to be 2570MHz. Bandwidth of both SI and SoI is set to 20MHz. By utilizing the adjacent band for the SoI, both the IQ Imbalance and the RSI (due to the insufficiency in nonlinear modelling) is omitted for the SoI band. Thus, for $\approx$ 10 dBm, $\approx$ 13 dBm, and $\approx$ 16.5 dBm average antenna transmit powers the demodulation performance of Adjacent-Band SoI is greater than the demodulation performance of the In-Band SoI as they are shown in Figures 5.9, 5.10, and 5.11, respectively.

Moreover, the IBFD spectral efficiency advantage over HD is still valid for Adjacent-Band SoI even though it occupies an additional band other than the SI band. This stems from the specific frequency band utilization of the Adjacent-Band SoI. It does not occupy any other band, it occupies the adjacent band of the SI that could have

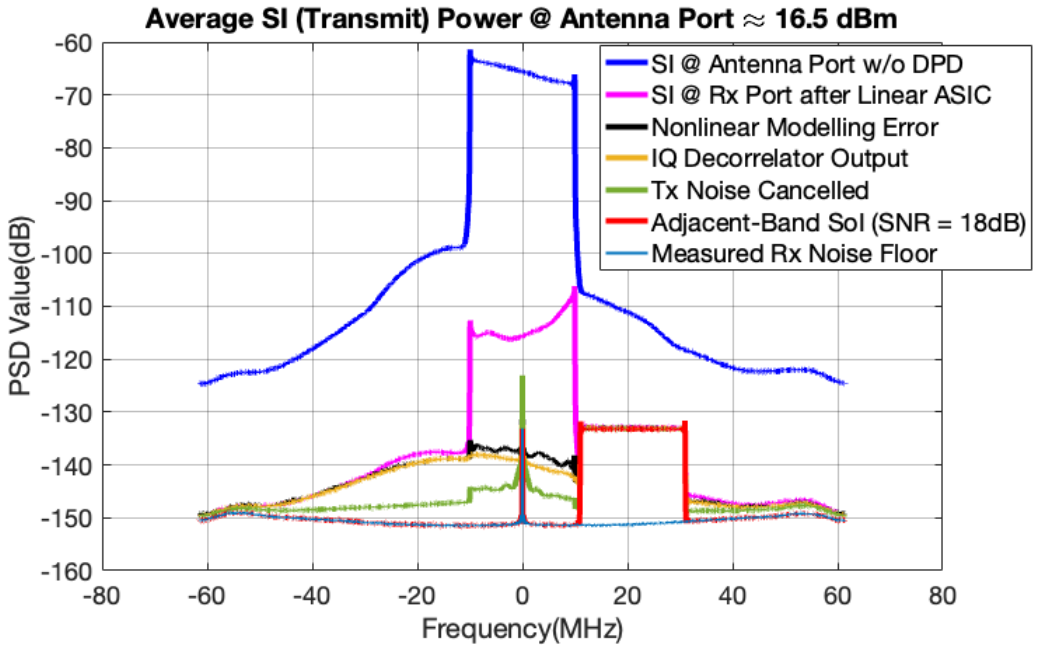

Figure 5.8: Adjacent-Band SoI is activated and SoI-SNR is set to 18 dB. SIC Summary in the spectrum after linear ASIC, nonlinear DSIC, IQ Decorrelator, and Noise Cancellation where the average antenna transmit power is $\approx$ 16.5 dBm.

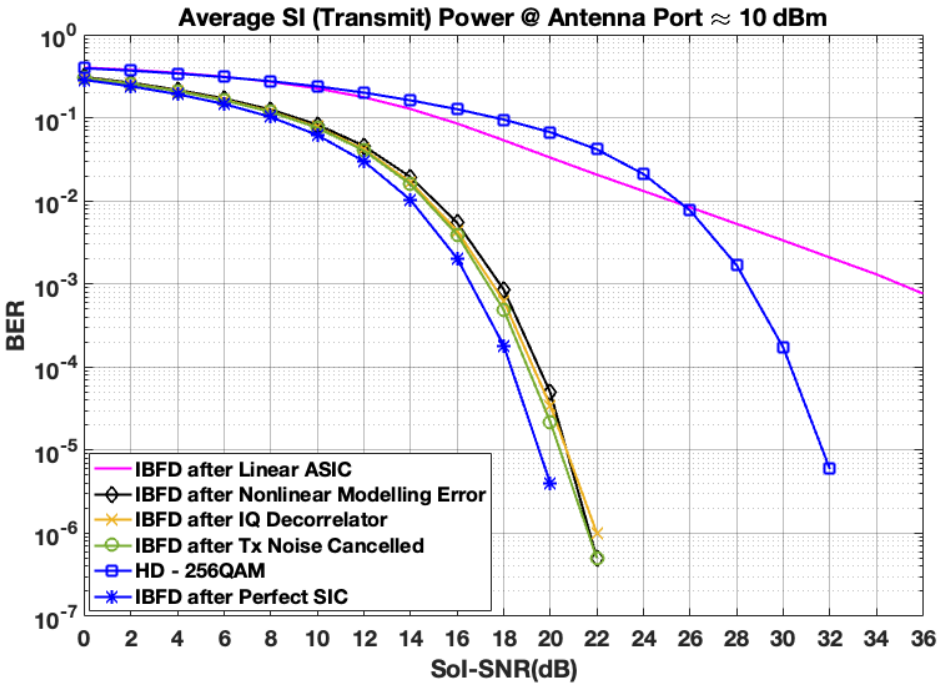

Figure 5.9: BER performance of the SIC algorithms for various Adjacent-Band SoI SNRs, where the average antenna transmit power is ≈ 10 dBm.

not been used due to the sidebands of the SI signal. However, by performing SIC, the adjacent band of the SI becomes available and it can be utilized by the Adjacent-Band SoI to double the spectral efficiency of the 16QAM IBFD system. Thus, the throughput-equivalent counterpart of the 16QAM IBFD system that utilizes Adjacent-Band SoI is still the 256QAM HD system.

In Figure 5.12, it is clearly shown that the Adjacent-Band SoI demodulation performance for ≈ 16.5 dBm average antenna transmit power is the same as the In-Band SoI demodulation performance for ≈ 10 dBm average antenna transmit power. This outcome results from Figure 5.8. The RSI in the in-band of SI does not affect the Adjacent-Band SoI and increase the receiver noise floor for the Adjacent-Band SoI demodulation.

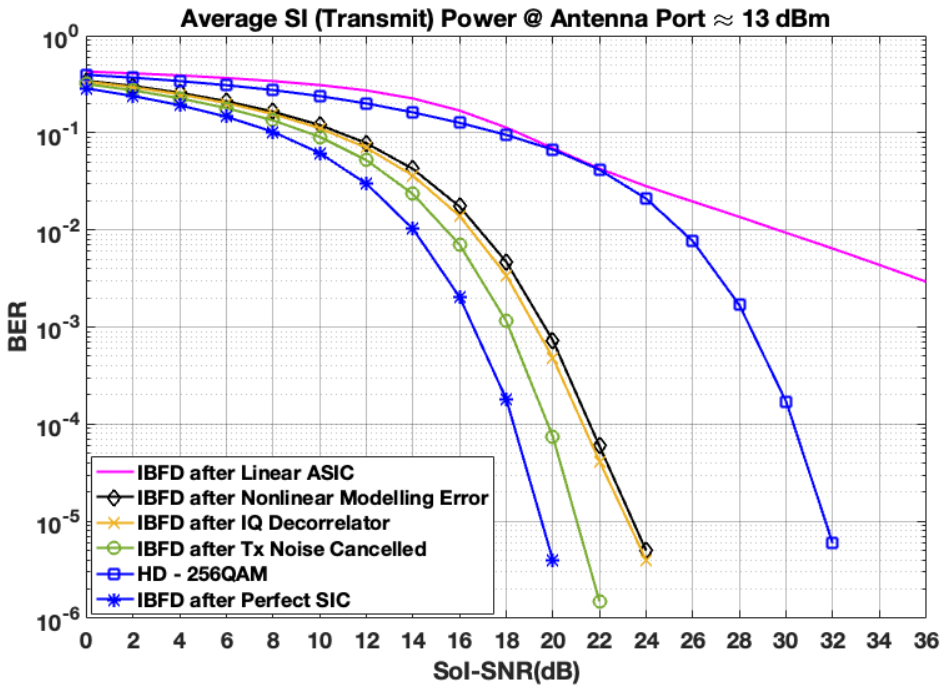

Figure 5.10: BER performance of the SIC algorithms for various Adjacent-Band SoI SNRs, where the average antenna transmit power is ≈ 13 dBm.

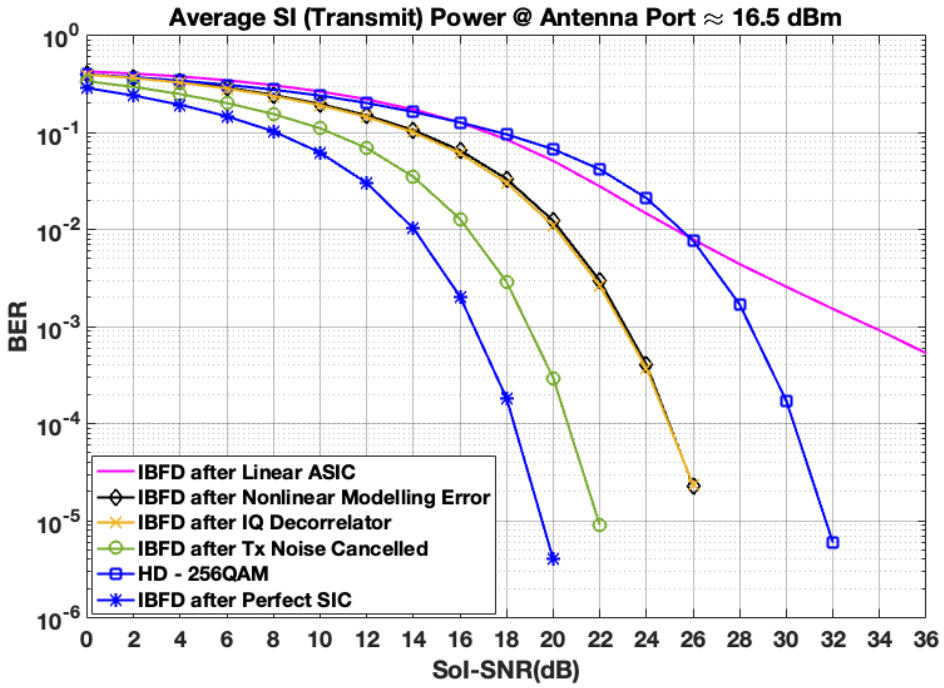

Figure 5.11: BER performance of the SIC algorithms for various Adjacent-Band SoI SNRs, where the average antenna transmit power is ≈ 16.5 dBm.

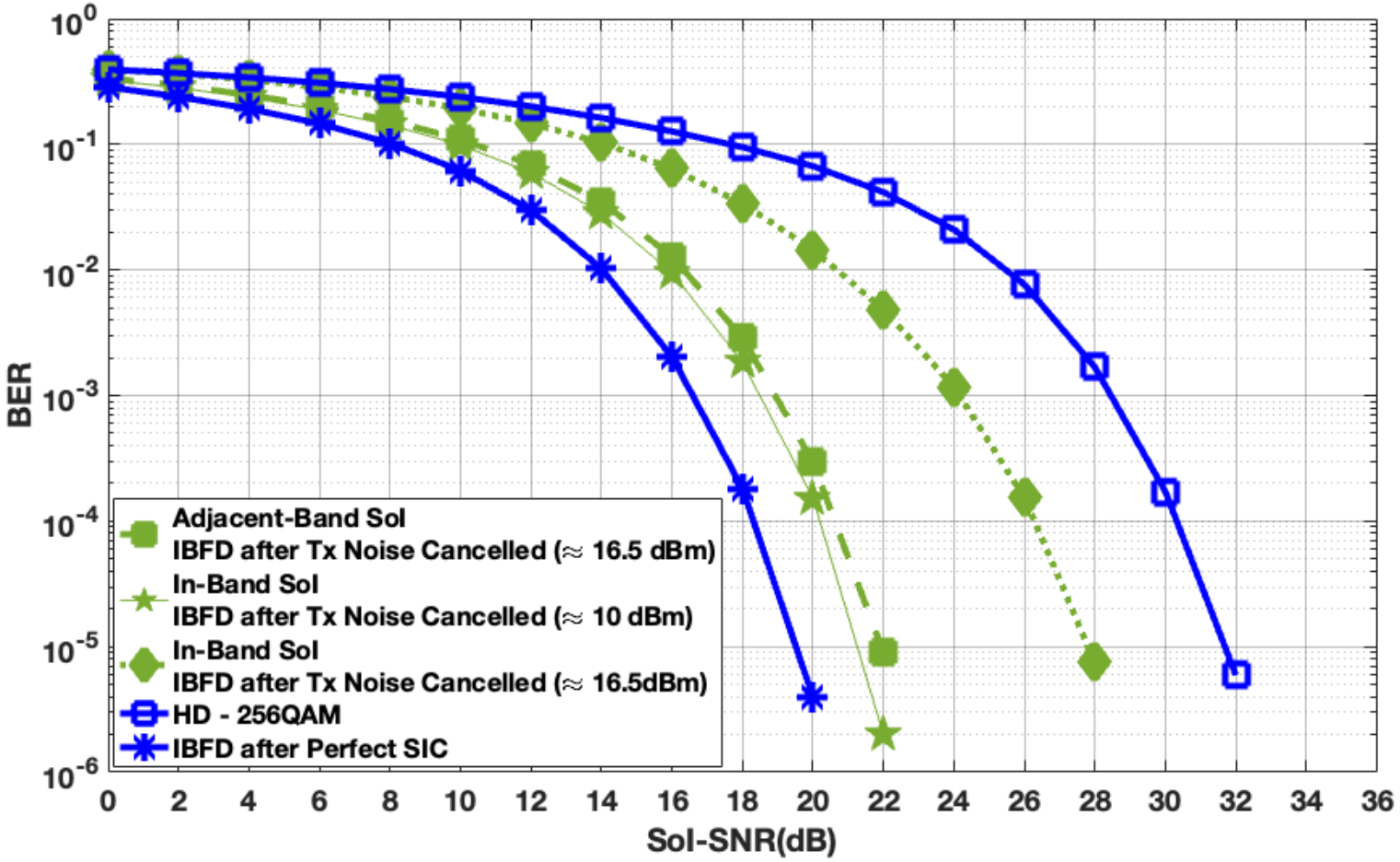

Figure 5.12: BER comparison of SIC algorithms operating in different average antenna transmit powers for various Adjacent-Band and In-Band SoI SNRs.

CHAPTER 6

CONCLUSION

In this thesis, previously proposed linear ASIC, nonlinear DSIC algorithms in [11] are rederived and recently proposed IQ Decorrelator algorithm is derived under OFDM signal model in Chapter 2. Furthermore in Chapter 2, the nonlinear single-antenna hardware setup is introduced and the mentioned SIC algorithms are evaluated on the SI signal for $\approx$ 10 dBm average antenna transmit power and observed that the P_{RSI} level is close to the measured receiver noise floor. In Chapter 3, the same SIC algorithms are evaluated for higher average antenna transmit powers, $\approx$ 13 dBm & $\approx$ 16.5 dBm, and observed that the discussed SIC algorithms become limited. Such a limitation is resulted in the discovery of the transmitter noise in the used hardware setup. Then in Chapter 4, the hardware setup is simulated in MATLAB with an addition of the transmitter noise and the limiting effect of the transmitter noise on the SIC algorithms is shown. Then, the observation channel is utilized to capture the same transmitter noise realization as the receiver channel and the Noise Cancellation algorithm is proposed in the simulation environment. When it is shown that the proposed noise cancellation algorithm can cancel the transmitter noise up to the receiver noise floor in the simulation, its performance is evaluated in the hardware setup. It is observed that the noise cancellation algorithm significantly improves the SIC performance at higher average antenna transmit powers. However, it is also observed that some RSI is left both in the in-band and out-of-band spectrum. It is concluded that the nonlinear DSIC based on GMP is insufficient to model the nonlinear characteristic of the PA especially in higher average antenna transmit powers. Nevertheless in Chapter 5, In-Band SoI & Adjacent-Band SoI are separately activated and BER versus SoI-SNR performance of the SIC algorithms alongside with Noise Cancellation on different average antenna transmit powers is calculated. Two benchmarks are

employed in BER analysis to compare the performances: 16QAM IBFD with perfect SIC and 256QAM HD. The former is used to compare how the proposed SIC algorithms perform and how the bottlenecks affect the performance. The latter is used to decide whether the IBFD system should be employed or not, as 256QAM HD is the $2\times$ throughput counterpart of the 16QAM IBFD. When In-Band SoI is employed, is it clearly shown that the proposed Noise Cancellation algorithm makes the 16QAM IBFD more favorable than the throughput-equivalent 256QAM HD for all the average antenna transmit powers that the used hardware setup supports. When Adjacent-Band SoI is employed, BER performance of the Noise Cancellation algorithm is further improved as RSI in the in-band of the SI is omitted. It is clearly shown that the Adjacent-Band SoI BER performance for $\approx$ 16.5 dBm average antenna transmit power is the same as the In-Band SoI BER performance for $\approx$ 10dBm average antenna transmit power.

Two future works have already been planned: (i) Using real-valued time-delay neural networks (RVTDNN) in nonlinear DSIC rather than the GMP based nonlinear modelling and (ii) Using RVTDNN both in nonlinear DSIC and Noise Cancellation algorithms. It is clear that the proposed nonlinear modelling left a significant P_{RSI} at the end of the SIC algorithm, especially in higher average antenna powers. GMP is a simplified version of Volterra Series Expansions of nonlinear systems based on Hammerstein models [44] and these architectures are not capable of modelling complex nonlinear systems especially those exposed to memory effects in wideband systems [45]. Furthermore, as it is stated in [11], a RVTDNN decouples the input and output relations of real and imaginary parts. Thus in the presence of a RVTDNN in the nonlinear modelling DSP block, the IQ Decorrelator DSP block can be discarded. Last but not least, RVTDNN based Noise Cancellation algorithm can be tailored to operate in a FPGA based IBFD node without MATLAB support for deployability with a very low resource utilization [45].

REFERENCES

[1] A. Goldsmith, *Wireless Communications*. New York, NY, USA: Cambridge University Press, 2005.

[2] F.-L. Luo and C. Zhang, *Signal Processing for 5G: Algorithms and Implementations*. Wiley-IEEE Press, 2016.

[3] D. Ince, *A Dictionary of the Internet*. Oxford University Press, 2nd ed., 2009.

[4] Y. Liao, L. Song, Z. Han, and Y. Li, "Full duplex cognitive radio: A new design paradigm for enhancing spectrum usage," *IEEE Communications Magazine*, vol. 53, no. 5, pp. 138–145, 2015.

[5] Z. Zhang, X. Chai, K. Long, A. V. Vasilakos, and L. Hanzo, "Full duplex techniques for 5G networks: Self-interference cancellation, protocol design, and relay selection," *IEEE Communications Magazine*, vol. 53, no. 5, pp. 128–137, 2015.

[6] L. Wang, F. Tian, T. Svensson, D. Feng, M. Song, and S. Li, "Exploiting full duplex for device-to-device communications in heterogeneous networks," *IEEE Communications Magazine*, vol. 53, no. 5, pp. 146–152, 2015.

[7] S. Hong, J. Brand, J. I. Choi, M. Jain, J. Mehlman, S. Katti, and P. Levis, "Applications of self-interference cancellation in 5G and beyond," *IEEE Communications Magazine*, vol. 52, no. 2, pp. 114–121, 2014.

[8] J. I. Choi, M. Jain, K. Srinivasan, P. Levis, and S. Katti, "Achieving single channel, full duplex wireless communication," in *Proceedings of the Sixteenth Annual International Conference on Mobile Computing and Networking*, MobiCom '10, (New York, NY, USA), p. 1–12, Association for Computing Machinery, 2010.

[9] B. Radunovic, D. Gunawardena, A. Proutiere, N. Singh, V. Balan, and P. Key, "Efficiency and fairness in distributed wireless networks through self-

interference cancellation and scheduling," in *Technical Report MSR-TR-2009-27*, Microsoft Research, 2009.

[10] M. Jain, J. I. Choi, T. Kim, D. Bharadia, S. Seth, K. Srinivasan, P. Levis, S. Katti, and P. Sinha, "Practical, real-time, full duplex wireless," in *Proceedings of the 17th Annual International Conference on Mobile Computing and Networking (MobiCom)*, p. 301–312, 2011.

[11] A. Kurt, M. B. Salman, H. A. Satana, and G. M. Guvensen, "An efficient iterative SIC for full-duplex SC-FDE radio under hardware impairments," in *ICC 2021 - IEEE International Conference on Communications*, pp. 1–6, 2021.

[12] D. Bharadia, E. McMilin, and S. Katti, "Full duplex radios," *SIGCOMM Comput. Commun. Rev.*, vol. 43, no. 4, p. 375–386, 2013.

[13] M. Duarte and A. Sabharwal, "Full-duplex wireless communications using off-the-shelf radios: Feasibility and first results," in *2010 Conference Record of the Forty Fourth Asilomar Conference on Signals, Systems and Computers*, pp. 1558–1562, 2010.

[14] E. Everett, M. Duarte, C. Dick, and A. Sabharwal, "Empowering full-duplex wireless communication by exploiting directional diversity," in *2011 Conference Record of the Forty Fifth Asilomar Conference on Signals, Systems and Computers (ASILOMAR)*, pp. 2002–2006, 2011.

[15] R. Askar, T. Kaiser, B. Schubert, T. Haustein, and W. Keusgen, "Active self-interference cancellation mechanism for full-duplex wireless transceivers," in *2014 9th International Conference on Cognitive Radio Oriented Wireless Networks and Communications (CROWNCOM)*, pp. 539–544, 2014.

[16] M. A. Khojastepour, K. Sundaresan, S. Rangarajan, X. Zhang, and S. Barghi, "The case for antenna cancellation for scalable full-duplex wireless communications," in *Proceedings of the 10th ACM Workshop on Hot Topics in Networks*, pp. 17:1–17:6, Association for Computing Machinery, 2011.

[17] E. Everett, A. Sahai, and A. Sabharwal, "Passive self-interference suppression for full-duplex infrastructure nodes," *CoRR*, vol. abs/1302.2185, 2013.

[18] A. Sabharwal, P. Schniter, D. Guo, D. W. Bliss, S. Rangarajan, and R. Wichman, "In-band full-duplex wireless: Challenges and opportunities," *IEEE Journal on Selected Areas in Communications*, vol. 32, no. 9, pp. 1637–1652, 2014.

[19] B. P. Day, A. R. Margetts, D. W. Bliss, and P. Schniter, "Full-duplex bidirectional MIMO: Achievable rates under limited dynamic range," *IEEE Transactions on Signal Processing*, vol. 60, no. 7, pp. 3702–3713, 2012.

[20] D. Korpi, L. Anttila, and M. Valkama, "Feasibility of in-band full-duplex radio transceivers with imperfect RF components: Analysis and enhanced cancellation algorithms," in *2014 9th International Conference on Cognitive Radio Oriented Wireless Networks and Communications (CROWNCOM)*, pp. 532–538, 2014.

[21] "MAFR-000229 single junction surface mount circulator," in *data sheet*, M/A-COM Technology Solutions Inc.

[22] Y. Hua, Y. Ma, P. Liang, and A. Cirik, "Breaking the barrier of transmission noise in full-duplex radio," in *MILCOM 2013 - 2013 IEEE Military Communications Conference*, pp. 1558–1563, 2013.

[23] E. Ahmed and A. M. Eltawil, "All-digital self-interference cancellation technique for full-duplex systems," *IEEE Transactions on Wireless Communications*, vol. 14, no. 7, pp. 3519–3532, 2015.

[24] D. Korpi, T. Riihonen, V. Syrjälä, L. Anttila, M. Valkama, and R. Wichman, "Full-duplex transceiver system calculations: Analysis of ADC and linearity challenges," *IEEE Transactions on Wireless Communications*, vol. 13, no. 7, pp. 3821–3836, 2014.

[25] L. Anttila, D. Korpi, V. Syrjälä, and M. Valkama, "Cancellation of power amplifier induced nonlinear self-interference in full-duplex transceivers," in *2013 Asilomar Conference on Signals, Systems and Computers*, pp. 1193–1198, 2013.

[26] S. Li and R. D. Murch, "Full-duplex wireless communication using transmitter output based echo cancellation," in *2011 IEEE Global Telecommunications Conference - GLOBECOM 2011*, pp. 1–5, 2011.

[27] D. Morgan, Z. Ma, J. Kim, M. Zierdt, and J. Pastalan, "A generalized memory polynomial model for digital predistortion of RF power amplifiers," *IEEE Transactions on Signal Processing*, vol. 54, no. 10, pp. 3852–3860, 2006.

[28] L. Anttila, D. Korpi, E. Antonio-Rodríguez, R. Wichman, and M. Valkama, "Modeling and efficient cancellation of nonlinear self-interference in MIMO full-duplex transceivers," in *2014 IEEE Globecom Workshops (GC Wkshps)*, pp. 777–783, 2014.

[29] K. Komatsu, Y. Miyaji, and H. Uehara, "Iterative nonlinear self-interference cancellation for in-band full-duplex wireless communications under mixer imbalance and amplifier nonlinearity," *IEEE Transactions on Wireless Communications*, vol. 19, no. 7, pp. 4424–4438, 2020.

[30] K. Komatsu, Y. Miyaji, and H. Uehara, "Basis function selection of frequency-domain Hammerstein self-interference canceller for in-band full-duplex wireless communications," *IEEE Transactions on Wireless Communications*, vol. 17, no. 6, pp. 3768–3780, 2018.

[31] A. Kaya and G. M. Guvensen, "A circular postamble structure enabling low complexity equalization in frequency domain for noncausal channels: Cyclic suffix," in *2020 28th Signal Processing and Communications Applications Conference (SIU)*, pp. 1–4, 2020.

[32] "OFDM raised cosine windowing," in *N7617A Signal Studio for 802.11 WLAN Online Document*, Agilent Technologies, 2009.

[33] S. K. Sharma, T. E. Bogale, L. B. Le, S. Chatzinotas, X. Wang, and B. Ottersten, "Dynamic spectrum sharing in 5G wireless networks with full-duplex technology: Recent advances and research challenges," *IEEE Communications Surveys & Tutorials*, vol. 20, no. 1, pp. 674–707, 2018.

[34] A. Sabharwal, P. Schniter, D. Guo, D. W. Bliss, S. Rangarajan, and R. Wichman, "In-band full-duplex wireless: Challenges and opportunities," *IEEE Journal on Selected Areas in Communications*, vol. 32, no. 9, pp. 1637–1652, 2014.

[35] "Datasheet," in *AD9683 Datasheet*, Analog Devices Inc., 2014.

[36] D. Kim, H. Lee, and D. Hong, "A survey of in-band full-duplex transmission: From the perspective of PHY and MAC layers," *IEEE Communications Surveys & Tutorials*, vol. 17, no. 4, pp. 2017–2046, 2015.

[37] "Ug-992," in *AD9371/AD9375 System Development User Guide*, Analog Devices Inc., 2016.

[38] F. J. Soriano-Irigaray, J. S. Fernandez-Prat, F. J. Lopez-Martinez, E. Martos-Naya, O. Cobos-Morales, and J. T. Entrambasaguas, "Adaptive self-interference cancellation for full duplex radio: Analytical model and experimental validation," *IEEE Access*, vol. 6, pp. 65018–65026, 2018.

[39] "Datasheet," in *AD9375 Datasheet*, Analog Devices Inc., 2016.

[40] "Datasheet," in *ADF4372 Datasheet*, Analog Devices Inc., 2019.

[41] "Datasheet," in *SKY66397-12 Datasheet*, Skyworks Solutions Inc., 2019.

[42] "Datasheet," in *SKY67189-396LF Datasheet*, Skyworks Solutions Inc., 2021.

[43] A. Saleh, "Frequency-independent and frequency-dependent nonlinear models of TWT amplifiers," *IEEE Transactions on Communications*, vol. 29, no. 11, pp. 1715–1720, 1981.

[44] F.-L. Luo, ed., *Digital Front-End in Wireless Communications and Broadcasting: Circuits and Signal Processing*. Cambridge University Press, 2011.

[45] S. Yeşil, C. Şen, and A. O. Yılmaz, "Experimental analysis and FPGA implementation of the real valued time delay neural network based digital predistortion," in *2019 26th IEEE International Conference on Electronics, Circuits and Systems (ICECS)*, pp. 614–617, 2019.

Appendix A

GENERALIZED MEMORY POLYNOMIAL

Hammerstein nonlinearity model is formed by a nonlinearity followed by a LTI filter. It can be expressed as in (A.1), mathematically:

$$y_H(n) = \sum_{m=0}^{M-1} g(m) \sum_{k=0}^{K-1} a_k x^k(n-m), \tag{A.1}$$

where x is an input signal, a_k are the polynomial coefficients of the nonlinearity, and g is a causal linear filter. Hammerstein model shown in (A.1) can be generalized by narrowband representation and choosing different filters for each different order k. It is called as memory polynomial [27] and can be shown in (A.2):

$$y_{MP}(n) = \sum_{k=0}^{K-1} \sum_{m=0}^{M-1} a_{km} x(n-m)|x(n-m)|^k, \tag{A.2}$$

where two dimensional array $\{a_{km}\}$ combines different filters and power series coefficients. As a limitation, the products in (A.2) involve input samples at the same time. To generalize and introduce cross terms in (A.2) the equation is rewritten as in (A.3):

$$\sum_{k=0}^{K-1} \sum_{m=1}^{M-1} b_{km} x(n)|x(n-m)|^k. \tag{A.3}$$

When multiple positive (leading envelope) and negative (lagging envelope) cross term time shifts are taken, it is known as generalized memory polynomial [27] and can be written as in (A.4):

$$
\begin{aligned}
y_{GMP}(n) = & \sum_{k\in\mathcal{K}_a}\sum_{l\in\mathcal{L}_a} a_{kl}x(n-l)|x(n-l)|^k \\
& + \sum_{k\in\mathcal{K}_b}\sum_{l\in\mathcal{L}_b}\sum_{m\in\mathcal{M}_b} b_{klm}x(n-l)|x(n-l-m)|^k \\
& + \sum_{k\in\mathcal{K}_c}\sum_{l\in\mathcal{L}_c}\sum_{m\in\mathcal{M}_c} c_{klm}x(n-l)|x(n-l+m)|^k,
\end{aligned}
\tag{A.4}
$$

where $\mathcal{K}_a$ & $\mathcal{L}_a$, $\mathcal{K}_b$ & $\mathcal{L}_b$ & $\mathcal{M}_b$, and $\mathcal{K}_c$ & $\mathcal{L}_c$ & $\mathcal{M}_c$ running indices are used to involve aligned, lagging, and leading signal envelopes, respectively.

Appendix B

IQ IMBALANCE

A direct conversion transmitter/receiver uses two quadrature sinusoidal signals to up-/down convert the signal from baseband to passband and from passband to baseband, respectively. Ideally, two quadrature sinusoidal signals should not have any phase and amplitude differences [2]. However, in practical systems some mismatch can be found either in amplitude, phase or both. Suppose both the amplitude (g^{Tx}) and phase (ϕ^{Tx}) mismatch occurs in the upconversion mixers, as it is shown in (B.1):

$$\begin{aligned} x_{LO}^{Tx}(t) &= \cos(2\pi f_c t) + jg^{Tx}\sin(2\pi f_c t + \phi^{Tx}), \\ &= \left(\frac{\mathrm{e}^{j2\pi f_c t} + \mathrm{e}^{-j2\pi f_c t}}{2}\right) + jg^{Tx}\left(\frac{\mathrm{e}^{j(2\pi f_c t+\phi^{Tx})} - \mathrm{e}^{-j(2\pi f_c t+\phi^{Tx})}}{2}\right), \\ &= \mathrm{e}^{j2\pi f_c t}\left(\frac{1 + g^{Tx}\mathrm{e}^{j\phi^{Tx}}}{2}\right) + \mathrm{e}^{-j2\pi f_c t}\left(\frac{1 - g^{Tx}\mathrm{e}^{-j\phi^{Tx}}}{2}\right), \end{aligned} \tag{B.1}$$

where $K_1 \triangleq \left(\frac{1+g^{Tx}\mathrm{e}^{j\phi^{Tx}}}{2}\right)$ and $K_2 \triangleq \left(\frac{1-g^{Tx}\mathrm{e}^{-j\phi^{Tx}}}{2}\right)$ are real-valued scalars. Then, baseband signal $x_{BB}(t) = x_I(t) + jx_Q(t)$ can be multiplied with the transmit LO to generate the transmitted signal, as in (B.2):

$$\begin{aligned} y(t) &= Re\Big\{x_{BB}(t)x_{LO}^{Tx}(t)\Big\}, \\ &= Re\Big\{x_{BB}(t)K_1\mathrm{e}^{j2\pi f_c t}\Big\} + Re\Big\{x_{BB}(t)K_2\mathrm{e}^{-j2\pi f_c t}\Big\}, \\ &= Re\Big\{x_{BB}(t)K_1\mathrm{e}^{j2\pi f_c t}\Big\} + Re\Big\{x_{BB}^{*}(t)K_2\mathrm{e}^{j2\pi f_c t}\Big\}, \end{aligned} \tag{B.2}$$

where $x_{BB}^{*}(t)$ denotes the complex conjugate of $x_{BB}(t)$. Then, the time and frequency domain baseband equivalent transmit signals which suffer from the transmit-

ter IQ Imbalance can be written as in (B.3) and (B.4), respectively:

$$y_{BB}(t) = K_1 x_{BB}(t) + K_2 x^*_{BB}(t) \tag{B.3}$$

$$Y_{BB}[k] = K_1 X_{BB}[k] + K_2 X^*_{BB}[-k] \tag{B.4}$$

Transmitter IQ Imbalance can be easily extended to receiver IQ Imbalance. In fact, in Section 2.4, the Inter-Carrier Interference caused by transmitter and receiver IQ Imbalance is shown in Figure 2.9.